The Astronomical Journal, 169:23 (18pp), 2025 January https://doi.org/10.3847/1538-3881/ad8dde

The HUSTLE Program: The UV to Near-infrared HST WFC3/UVIS G280 Transmission Spectrum of WASP-127b

V. A. Boehm[1], N. K. Lewis[1], C. E. Fairman[2], S. E. Moran[3], C. Gascón[4,5], H. R. Wakeford[2], M. K. Alam[6], L. Alderson[2], J. Barstow[7], N. E. Batalha[8], D. Grant[2], M. López-Morales[4], R. J. MacDonald[9,11], Mark S. Marley[3], and K. Ohno[10]
[1] Department of Astronomy, Cornell University, 122 Sciences Drive, Ithaca, NY 14853, USA; vab55@cornell.edu
[2] School of Physics, University of Bristol, H.H. Wills Physics Laboratory, Tyndall Avenue, Bristol BS8 1TL, UK
[3] Department of Planetary Sciences and Lunar and Planetary Laboratory, University of Arizona, Tuscon, AZ 85721, USA
[4] Center for Astrophysics | Harvard & Smithsonian, 60 Garden Street, Cambridge, MA 02138, USA
[5] Institut d'Estudis Espacials de Catalunya (IEEC), 08860 Castelldefels (Barcelona), Spain
[6] Space Telescope Science Institute, 3700 San Martin Drive, Baltimore, MD 21218, USA
[7] School of Physical Sciences, The Open University, Walton Hall, Milton Keynes MK7 6AA, UK
[8] NASA Ames Research Center, Moffett Field, CA 94035, USA
[9] Department of Astronomy, University of Michigan, 1085 S. University Avenue, Ann Arbor, MI 48109, USA
[10] Department of Astronomy and Astrophysics, University of California, Santa Cruz, CA, USA
Received 2024 July 16; revised 2024 September 23; accepted 2024 October 12; published 2024 December 12

Abstract

Ultraviolet wavelengths offer unique insights into aerosols in exoplanetary atmospheres. However, only a handful of exoplanets have been observed in the ultraviolet to date. Here, we present the ultraviolet-visible transmission spectrum of the inflated hot Jupiter WASP-127b. We observed one transit of WASP-127b with WFC3/UVIS G280 as part of the Hubble Ultraviolet-optical Survey of Transiting Legacy Exoplanets, obtaining a transmission spectrum from 200 to 800 nm. Our reductions yielded a broadband transit depth precision of 91 ppm and a median precision of 240 ppm across 59 spectral channels. Our observations are suggestive of a high-altitude cloud layer with forward modeling showing they are composed of submicron particles and retrievals indicating a high-opacity patchy cloud. While our UVIS/G280 data only offer weak evidence for Na, adding archival Hubble Space Telescope (HST) WFC3/IR and STIS observations raises the overall Na detection significance to 4.1σ. Our work demonstrates the capabilities of HST WFC3/UVIS G280 observations to probe the aerosols and atmospheric composition of transiting hot Jupiters with comparable precision to HST STIS.

Unified Astronomy Thesaurus concepts: Exoplanets (498); Exoplanet atmospheres (487); Extrasolar gaseous giant planets (509); Transmission spectroscopy (2133)

1. Introduction

The past decade of research into the atmospheres of transiting hot Jupiters has made thorough use of the Hubble Space Telescope (HST) and its Wide Field Camera 3 (WFC3) infrared (IR) channel and the Space Telescope Imaging Spectrograph (STIS). In particular, studies regularly made use of the STIS G430L and G750L gratings (300–1050 nm) and the WFC3/IR G141 grism (1100–1600 nm). Observations in these modes were sometimes supplemented with the WFC3/IR G102 grism (800–1100 nm) to bridge the gap between STIS and WFC3/IR (see, e.g., F. Pont et al. 2013; D. K. Sing et al. 2015; H. R. Wakeford et al. 2018; J. J. Spake et al. 2021). Additionally, the high-resolution echelle gratings (e.g., STIS E230M; see D. K. Sing et al. 2019) were also used to probe escaping atmospheres. By combining multiple transit observations, each taken through a different mode, a detailed transmission spectrum spanning 300–1700 nm could be built up. However, as this observing strategy requires multiple transits, it can be subject to variability in instrumental systematics and stellar activity across visits.

The commonly used HST observing modes barely measure ultraviolet (UV) spectra of exoplanet atmospheres (100–400 nm). The near- (300–400 nm) and mid-UV (200–300 nm) spectra of hot Jupiters are an underutilized probe of atmospheric aerosols, as short-UV wavelengths show particularly strong signatures of Rayleigh scattering caused by nanometer-to-micrometer-scale particles (e.g., K. Ohno & Y. Kawashima 2020). Furthermore, the UV wavelengths cover a range of strongly absorbing gases and molecules such as silicate oxide vapor (e.g., J. D. Lothringer et al. 2022) or mineral condensates (e.g., H. R. Wakeford & D. K. Sing 2015), which are important for overall atmospheric chemistry.

The HST WFC3/UVIS G280 grism is an ultraviolet-visible (UVIS) grism that went largely unused by the exoplanetary science community until recently. H. R. Wakeford et al. (2020) demonstrated WFC3/UVIS G280's capabilities for exoplanet characterization via a proof-of-concept study on the hot Jupiter HAT-P-41b. Several unusual features of UVIS/G280 make it challenging to work with, in particular its strongly curving traces and its higher orders that overlap the lower orders and introduce (typically minor) spectral self-contamination. Nevertheless, H. R. Wakeford et al. (2020) and additional studies (e.g., J. D. Lothringer et al. 2022) have proven that, despite these quirks, UVIS/G280 can produce reliable observations in the near- and mid-UV that make it worth the challenge. The spectral range of the UVIS/G280 grism (200–800 nm), which can be covered in just one transit observation, is comparable to

[11] NHFP Sagan Fellow.

the combined spectral range of both the STIS G430L and G750L instruments (300–1050 nm), which require at least two transit observations to acquire. UVIS/G280 also has superior throughput from 200 to 300 nm when compared to other HST modes, enabling us to constrain exoplanet cloud properties and atmospheric escape processes more robustly than has been done with other instruments. The proof-of-concept study presented in H. R. Wakeford et al. (2020) set the groundwork for the Hubble Ultraviolet-optical Survey of Transiting Legacy Exoplanets (HUSTLE) program, an ongoing HST treasury program observing 12 hot Jupiters using WFC3/UVIS G280 to probe transitions in atmospheric chemistry and structure across equilibrium temperatures spanning 960–2640 K (H. Wakeford et al. 2022).

As part of HUSTLE, we obtained observations of the hot Jupiter WASP-127b through UVIS/G280. WASP-127b is a $T_{\rm eq} = 1400 \pm 24$ K hot Jupiter with a highly inflated radius of $R_p = 1.37 \pm 0.04 R_J$, despite being less massive than Saturn at $M_p = 0.18 \pm 0.02 M_J$ (K. W. F. Lam et al. 2017). The scale height of its atmosphere is predicted to be in excess of 2000 km (J. J. Spake et al. 2021), one of the largest yet discovered. WASP-127b orbits a $V \sim 10.2$, photometrically quiet G-dwarf star (K. W. F. Lam et al. 2017). The host star's brightness and low activity level, combined with the large expected atmospheric scale height of the planet, make WASP-127b an ideal target for UVIS transmission spectroscopy. Furthermore, several studies posit that, at $T_{\rm eq} \sim 1400$ K, hot Jupiters and brown dwarfs may undergo a transition in aerosol structure, wherein silicate clouds begin to subside and manganese sulfide clouds (MnS) begin to condense in the upper atmosphere (e.g., C. V. Morley et al. 2012; V. Parmentier et al. 2016; H. R. Wakeford et al. 2017). By contrast, microphysics studies (e.g., P. Gao et al. 2020) suggest that energy barriers will inhibit the nucleation of MnS condensates so that MnS clouds should not be expected to be dominant on WASP-127b. Studies of this world with UVIS/G280 can constrain the nature of the clouds in its atmosphere, which will serve as a test of whether there is a transition from silicate clouds to MnS clouds near 1400 K.

Previous studies have targeted WASP-127b using data from both ground-based instruments—such as the Nordic Optical Telescope (E. Palle et al. 2017), the Gran Telescopio Canarias (G. Chen et al. 2018), HARPS (J. Žák et al. 2019), and ESPRESSO (R. Allart et al. 2020)—and from space-based observations with HST (300–1700 nm), Spitzer photometry at 3.6 and 4.5 μm, and TESS broadband photometry in the red optical (N. Skaf et al. 2020; J. J. Spake et al. 2021). These efforts characterized the spectrum of WASP-127b down to 300 nm and found a rise in transit depth at wavelengths short of 560 nm, but all studies disagreed on the steepness of this rise. E. Palle et al. (2017) and G. Chen et al. (2018) found a super-Rayleigh slope. To our current knowledge, the super-Rayleigh slope could be explained only by photochemical hazes with vigorous vertical mixing (Y. Kawashima & M. Ikoma 2019; K. Ohno & Y. Kawashima 2020), optical and/or near-UV absorbers such as SH radical (T. M. Evans et al. 2018) and sulfide clouds (e.g., MnS; see A. Pinhas & N. Madhusudhan 2017), or uncorrected contamination by starspots (e.g., P. R. McCullough et al. 2014), although the last explanation is somewhat disfavored for WASP-127b by the star's reported quietness (K. W. F. Lam et al. 2017). By contrast, J. J. Spake et al. (2021) observed a shallower, sub-Rayleigh scattering slope. If their finding is true, it could considerably alter the interpretation of the spectrum, as there are several other possibilities to explain the sub-Rayleigh slope, including mineral clouds without any requirement for particular cloud compositions (e.g., A. Pinhas & N. Madhusudhan 2017; C. W. Ormel & M. Min 2019; D. Powell et al. 2019; K. Ohno et al. 2020), as well as photochemical hazes without vigorous atmospheric mixing, especially for soot-like haze compositions (e.g., P. Lavvas & T. Koskinen 2017; K. Ohno & Y. Kawashima 2020; M. E. Steinrueck et al. 2023).

Regarding the atmospheric compositions of WASP-127b, probes into the near-IR spectrum through WFC3/IR and Spitzer have indicated supersolar abundances of H_2O and the possible presence of either CO_2 or CO (N. Skaf et al. 2020; J. J. Spake et al. 2021). This was followed up with ground-based observations with SPIRou from 900 to 2500 nm, which found CO at subsolar abundances and an H_2O abundance closer to solar (A. Boucher et al. 2023). Ground-based spectroscopy spanning 400–1000 nm suggested the presence of alkali metals in the atmosphere of WASP-127b, such as sodium, lithium, and potassium (E. Palle et al. 2017; G. Chen et al. 2018; J. Žák et al. 2019; R. Allart et al. 2020); however, space-based spectroscopic studies that confirmed the presence of sodium found no definitive evidence of lithium or potassium (J. J. Spake et al. 2021), which can be contaminated by telluric absorption from the ground.

Our study expands on this narrative by using HST's WFC3/UVIS G280 observing mode to resolve the spectrum of WASP-127b down to 200 nm with increased near-UV precision. In doing so, we aim to place stronger constraints on the spectrum short of 560 nm, which will better reveal the nature of the aerosols responsible for the rise in transit depth at these wavelengths. Furthermore, the spectral range of HST's WFC3/UVIS G280 will allow for the reexamination of prior claims of sodium, lithium, and potassium in the atmosphere of WASP-127b. We jointly analyze our new WFC3/UVIS G280 spectrum alongside archival data from HST's STIS and WFC3/IR, and Spitzer photometry to probe WASP-127b's atmosphere from the mid-UV to the near-IR.

Our study is structured as follows. In Section 2, we present our observations, our data reduction strategies, and our methods for extracting transit light curves from these data. Section 3 presents the analysis of the extracted light curves, including fitting both broadband and spectroscopic light curves to extract the system parameters and transit spectrum. In Section 4, we present forward modeling and retrieval interpretations of these data, and, in Section 5, we discuss our results and their significance in the context of previous observations of WASP-127b. Section 6 summarizes our work in the context of both HUSTLE and exoplanet studies as a whole, with suggestions for further work on this topic.

2. Observations and Methods

2.1. HST WFC3/UVIS G280 Observations

We observed one transit of the target WASP-127b with the HST WFC3/UVIS G280 grism, which provides wavelength coverage from 200 to 800 nm. These data were taken from 21:10:59 UTC on 2023 February 13 to 04:33:44 on 2023 February 14 as part of visit 12 of GO 17183 (PI: Hannah Wakeford). The visit spanned five HST orbits centered on midtransit, with one orbit before and one after transit to ensure adequate pre- and post-transit baseline measurements.

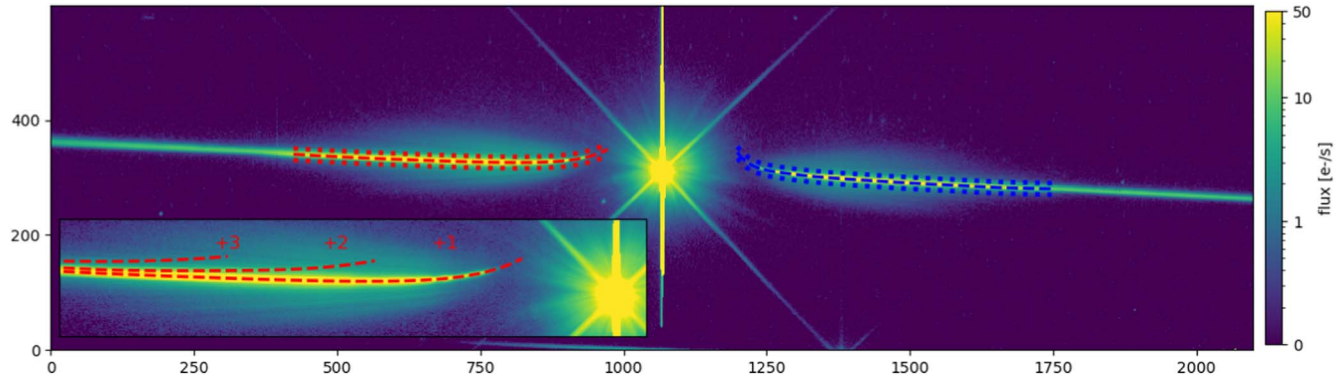

Figure 1. WASP-127 as seen through HST's WFC3/UVIS G280 grism. The saturated object seen at the center is the 0th order; the two diagonally crossing lines are diffraction spikes and thus an artifact of the optics, while the vertical line is bloom, an artifact of severe 0th-order saturation caused by electrons from very saturated pixels spilling out into vertically adjacent pixels. The gently swooping bright lines crossing the entire frame diagonally are the traces we aim to extract a spectrum from. To the left, the positive orders are dispersed, with the brightest and innermost trace being the +1st order. To the right, the negative orders are dispersed. Red (blue) dashed lines mark the `GRISMCONF` polynomial fits, and dotted lines mark the edges of the extraction aperture for the +1st (−1st) order. Background stars and their diffraction spikes/traces are faintly visible in some regions of the image; these do not affect our observations of WASP-127b. Inset: the first through third positive orders. Self-contamination at the level of 2% or less in the 1st order by the 2nd order begins at about 450 nm.

We collected 15 78 s frames in the first orbit and 16 frames in every subsequent orbit for a total of 79 frames and a 49% duty cycle. The strong curvature of UVIS/G280 traces required observations to be taken in stare mode, so no spatial scans were collected. Furthermore, because WFC3/UVIS uses a CCD detector, no nondestructive reads were available for analysis. Both the positive $m > 0$ and negative $m < 0$ orders of the trace were placed near the middle of chip 2 in a subarray region of dimensions 600×2100 out of the entire 2051×4096. Prior to UVIS/G280 measurements, a single frame was collected using the F300X UVIS filter to aid in wavelength calibration by measuring the exact position of the target in the custom subarray.

2.2. Data Reduction

To verify that the results we obtained with our analysis are grounded in truth and not artifacts of our reduction process, we processed our WASP-127b UVIS/G280 observations with two independent pipelines. Performing reductions of a data set with multiple pipelines allows one to disentangle which anomalies are intrinsic to the data and which are artifacts of the reduction process. In recent years, the importance of providing more than one reduction of a transit or eclipse observation using multiple distinct reduction pipelines has been recognized (see, e.g., JWST Transiting Exoplanet Community Early Release Science Team et al. 2023). We present here the HST WFC3/UVIS G280 pipeline `hazelnut` and detail it and its results in Section 2.2.1. We also present the results of a second UVIS/G280 pipeline, called `lluvia`, in Section 2.2.2.

2.2.1. `hazelnut`

Our `hazelnut` reduction followed the same procedures as detailed in H. R. Wakeford et al. (2020), which we describe briefly here. We started with the calibrated `flt` FITS files provided by MAST, which have been processed by the `calwfc3` pipeline to correct for dark current, read noise, and nonuniform pixel response. In contrast to WFC3/IR observations, for which the first orbit is strongly affected by systematics and must be discarded, WFC3/UVIS observations of the first orbit can be retained. However, previous works have found that, when using the WFC3/UVIS, the first frame of each orbit may present unusual high background values and value distributions, with an unknown cause suspected to be earthshine and/or systematics (H. R. Wakeford et al. 2020). Following their procedure, we discard each orbit's first frame. We then rejected cosmic rays and hot pixels from each frame in time and space. Cosmic rays were rejected from each pixel through a double iteration process over each pixel's time series. On each iteration, 4.5σ outliers in each time series were replaced with the median value of that pixel over the past three and next three frames, ensuring that in-transit outliers were replaced with in-transit values, not with out-of-transit signal. The threshold 4.5σ was determined by testing threshold values and selecting the lowest value that still produced a random spatial distribution of flagged outliers, since cosmic rays should hit the detector in a random way. About 8% of pixels were affected by this process. Hot pixels were rejected spatially through one iteration of Laplacian edge detection following P. G. van Dokkum (2001), with rejected pixels being replaced by the median of the pixels one space above, below, left, and right of it. We lastly removed the background sky signal by computing the mode count of each full frame and subtracting that value from the entire frame. As an example, we show in Figure 1 one of our time-series frames after the above cleaning procedures have been carried out.

Trace fitting was performed using the `GRISMCONF` software developed by N. Pirzkal & R. Ryan (2017), with the latest UVIS/G280 configurations provided by N. Pirzkal (2020). The direct image of WASP-127 obtained through the F300X filter was used to predict the position of the dispersed traces in UVIS/G280 images. From the position of the target in the F300X image, `GRISMCONF` fit a dispersion polynomial to the ±1st-, ±2nd-, ±3rd-, and ±4th-order traces in the UVIS/G280 images. The extracted stellar spectra contain Hα and Hβ absorption lines, from which we could confirm the accuracy of the dispersion polynomial to ±1 nm, just under 1 detector resolution element. `GRISMCONF` was used to assign a wavelength solution to the dispersion polynomial, which spans from 200 to beyond 800 nm; however, we truncated our analysis to the UVIS span from 202.5 to 792.5 nm. The lower bound was set by signal-to-noise ratio (SNR) constraints, while

the upper bound was determined by the onset of fringing effects that make reliable extraction impossible.

UVIS/G280 produces higher-order traces that contaminate the lower-order traces at long wavelengths. In particular, the ±2nd-order traces overlap with the ±1st-order traces, with the sharply curving UV edge of the 2nd-order trace overlapping the 1st-order trace around 400 nm. Self-contamination is thus present in all wavelengths redder than 400 nm. The severity of self-contamination is target dependent, being more significant for UV-bright host stars. In the case of WASP-127b, error due to photometric uncertainty was greater than error due to self-contamination, such that we treated self-contamination as negligible. However, we note that, for stars with more significant UV emission, self-contamination may require a more sophisticated treatment; we leave further discussion of how to treat this problem for other targets in the HUSTLE program.

We extracted our spectrum from an aperture that we defined as centered on the `GRISMCONF` polynomial fit and including all pixels within one half-width x above and below the fit. The preferred half-width should maximize signal while minimizing scatter accumulated from the background. This half-width was determined as follows:

1. Define the extraction aperture to be centered on the `GRISMCONF` dispersion polynomial fit and containing all pixels that are within one half-width x above and below the fit.
2. Perform simple unweighted extractions of the ±1st-order traces with apertures of half-width x ranging from 5 to 20 pixels, and sum to produce broadband light curves.
3. Fit a simple systematic model (linear trend + exponential ramp) to the out-of-transit flux and measure the scatter.
4. Select the half-width x that minimizes the out-of-transit scatter.

For this case, $x = 10$ was determined to be ideal.

Pointing instabilities in HST during observations lead to shifts of order tenths of pixels of the trace position on the detector over the course of a visit; however, the wavelength solution is fixed by the F300X direct image, leading to offsets in the wavelengths assigned to each frame's one-dimensional (1D) spectrum. To account for this offset, all 1D spectra were cross-correlated with the 1D spectrum extracted from frame 2 of orbit 1. Through cross-correlation, we measured spectral displacements and realigned all spectra to the frame 2 spectrum to ensure a consistent wavelength solution. A final round of cosmic-ray cleaning was then performed by comparing all spectra to the median spectrum and replacing 3.5σ outliers with the median value in time. Under 0.2% of 1D spectral points were deemed outliers at this stage with 72 total residual hits across both orders, as to be expected after undergoing the various cleaning treatments detailed above. Two extracted 1D spectra, one from the +1st order and one from the −1st order and both processed as described above, are presented in Figure 2.

We chose to extract our spectra from the +1st- and −1st-order traces as these orders have the highest SNR and widest wavelength coverage, while being the least affected by self-contamination from other spectral orders. We summed each order of 1D spectra across its entire spectral range to produce two broadband light curves, one per order. Spectroscopic light curves were produced from the 1D spectra by summing each

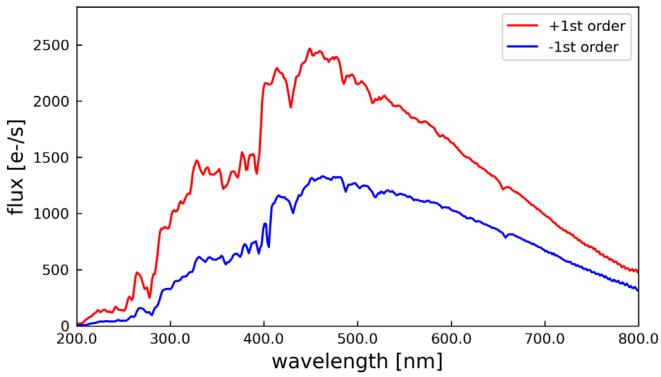

Figure 2. The +1st and −1st-order spectra obtained from our observations of WASP-127b through HST's WFC3/UVIS G280 grism. For the −1st order, there is insufficient flux short of 250 nm to perform a reliable analysis. Additionally, an unknown systematic between −1st-order wavelengths 397.5 nm and 407.5 nm created steep, spurious and untreatable jumps in flux level, which resulted in this region being excluded from further analysis.

spectrum across discrete wavelength bins with bin widths of 10 nm. From the brighter +1st order, 59 spectroscopic light curves spanning 202.5–792.5 nm were produced. The −1st order is considerably dimmer below 250 nm and has additional systematics between 397.5 nm and 407.5 nm, so only 52 spectroscopic light curves spanning 250–397.5 nm and 407.5–792.5 nm were produced from this order. In total, 111 spectroscopic light curves and two broadband light curves were produced for analysis, the details of which are provided in Section 3.

2.2.2. `lluvia`

`lluvia` is being developed independently of `hazelnut` and is detailed thoroughly in C. Gascon et al. (2024, in preparation); we provide a brief summary of its methods here along with its results. Our `lluvia` reduction likewise began with the `flt` FITS provided by MAST and calibrated by `calwfc3`, but retained all frames in each orbit including the first frames, in contrast to `hazelnut`. The background flux of each exposure was computed using four 150×400 pixel regions located in the four corners of the corresponding image. The central value of the histogram of counts across all four regions was then used as the image background. An initial cosmic-ray correction was performed on each image by iteratively identifying pixels that deviated by more than 5σ in time along each HST orbit, and replacing their flux values by the median pixel value of the corresponding orbit.

We calculated the position of both ±1 order spectral traces by fitting a Gaussian curve to each detector column (i.e., cross-dispersion direction), using the calibration trace obtained from the `GRISMCONF` package as an initial guess. We extracted the stellar spectra using the optimal extraction routine described in K. Horne (1986), with a ±10 pixel aperture around the center of the trace. To account for the curvature present in the traces of WFC3/UVIS G280, we built the spatial profile by fitting low-order polynomials along the trace direction, similar to the methodology proposed in T. R. Marsh (1989). We used this fitting process to perform a second cosmic-ray removal; pixels that deviated from the spatial profile model by more than 7σ were replaced by the corresponding value of the polynomial fit. We integrated the flux across the entire wavelength range to produce the ±1st-order broadband light curves. We also divided the extracted stellar spectra into 10 nm bins, to produce

Table 1
System Parameters Used for Fitting Broadband and Spectroscopic Transit Light Curves

Parameter	Value	Source
Stellar parameters		
Z ([Fe/H])	-0.18 ± 0.06	K. W. F. Lam et al. (2017)
$T_{\rm eff}$ (K)	5620 ± 85	K. W. F. Lam et al. (2017)
$\log(g)$ ($\log_{10}$(cm/s^2))	4.18 ± 0.01	K. W. F. Lam et al. (2017)
Exoplanet Parameters		
R_p/R_*	0.1000 ± 0.0004	This work
a/R_*	8.116 ± 0.106	This work
b	0.127 ± 0.062	This work
e	0.0	This work
P (days)	4.178062	J. J. Spake et al. (2021)
t_0 ($\rm BJD_{TDB}$)	2459989.546 ± 0.001	This work

Note. Stellar parameters were fixed from K. W. F. Lam et al. (2017). Exoplanet parameters were fitted by this analysis and derived from a weighted average of the MCMC fitting results from each order, except for the period P, which was fixed by J. J. Spake et al. (2021), and the eccentricity e, which we took to be 0.0.

a set of 57 spectral light curves for both ± 1 orders. The analysis of the broadband and spectroscopic light curves produced here is also detailed in Section 3.

3. Light-curve Fitting

3.1. hazelnut

3.1.1. Systematics Removal

Our hazelnut broadband and spectroscopic light curves were largely cleaned of outliers but were still affected by HST systematics, some of which were wavelength dependent. Thus, each light curve had to be individually treated for HST systematics. We did so through the ExoTiC-ISM package (I. Laginja & H. Wakeford 2020), the procedure behind which is detailed in H. R. Wakeford et al. (2016). ExoTiC-ISM fit a weighted combination of 51 systematics models to remove all known types of systematic trends found in our data, including HST thermal breathing, visit-long slopes, and ramp effects. We used ExoTiC-ISM to detrend all of our broadband and spectroscopic light curves before proceeding with further analysis.

3.1.2. Broadband Light-curve Analysis

We first analyzed our detrended broadband light curves spanning the entire spectral range of 202.5–792.5 nm. For each broadband light curve, we fit a K. Mandel & E. Agol (2002) transit model implemented through the batman Python package (L. Kreidberg 2015), with a four-parameter nonlinear stellar limb-darkening law. Fixed limb-darkening coefficients were generated by ExoTiC-LD (D. Grant & H. R. Wakeford 2024) using the ATLAS9 grid (D. Grant & H. R. Wakeford 2022). Our choice of 1D stellar model grid was motivated by consistency of comparison with J. J. Spake et al. (2024), but we note that our secondary reduction with lluvia uses a 3D grid instead. The stellar parameters we supplied to ExoTiC-LD are sourced from K. W. F. Lam et al. (2017) and reported in Table 1. Our fitting procedure is a two-step process that uses both linear and nonlinear fitting techniques. First, we used a scipy linear least-squares solver to fit a first-pass transit model, which includes a visit-long linear-in-time systematic trend. This model was used to revise our estimates of the photometric uncertainty as well as fit for the midtransit epoch T_0, the ratio of the semimajor axis to the host-star radius a/R_*, the impact parameter b, and the slope and y-intercept of the systematic. We then inputted the uncertainty estimates, systematic model, and the fitted values of T_0, a/R_*, and b to a routine that used EMCEE (D. Foreman-Mackey et al. 2013) to refit the transit model through a Markov Chain Monte Carlo (MCMC) algorithm with uninformed priors. We initialized our MCMC routine with planetary parameters from K. W. F. Lam et al. (2017) and ran 32 chains with 5000 steps each, discarding the first 640 steps (20% of each chain) as burn-in. We present a summary of the system parameters in Table 1, and in the left-side panels of Figure 3 we present the marginalized broadband light curves with fitted models and normalized residuals for each curve.

Our broadband light curves yielded a transit depth of $0.997\% \pm 0.009\%$ in the $+1$st order and $0.988\% \pm 0.016\%$ in the -1st order, for an overall depth precision of 91 ppm. Our $+1$st-order result is notably shallower than the G430L depth observed by J. J. Spake et al. (2021; $1.034^{+0.006}_{-0.005}\%$), within 2σ of their G750L depth ($1.013^{+0.009}_{-0.006}\%$), and agrees very well with their G141 depth ($0.996\% \pm 0.011\%$). We ascribe these differences primarily to changes in instrument systematics between visits, and apply offsets to the J. J. Spake et al. (2021) spectrum to align it with our own during the interpretation in Section 4. The -1st-order depth is notably more uncertain, as expected, since the negative orders are roughly half as bright as the positive orders. We fit system parameters separately for each order and combined our results in a weighted average, yielding orbit semimajor axis and impact parameter $a/R_* = 8.116 \pm 0.106$ and $b = 0.127 \pm 0.062$, consistent to 1σ with the values presented in K. W. F. Lam et al. (2017). Despite being fit separately, our $+1$st- and -1st-order fit parameters were also consistent to well within 1σ with each other. Our midtransit epoch was determined to be $T_0 = 2459989.546 \pm 0.001$ in $\rm BJD_{TDB}$. In our subsequent analysis of the spectroscopic transit curves, we fixed a/R_*, b, and T_0 to the values obtained here.

3.1.3. Spectroscopic Light-curves Analysis

We followed a very similar analysis procedure for the spectroscopic light curves, first using a linear least-squares fit to update the photometric uncertainty estimates and then using MCMC to derive a final fit with uncertainty estimates on the fitted parameters. We fit a transit model with a linear-in-time systematic and fixed limb-darkening coefficients generated for each wavelength bin by ExoTiC-LD with a four-parameter nonlinear limb-darkening law. As before, ATLAS9 grid coefficients were supplied by ExoTiC-LD, and stellar parameters were sourced from K. W. F. Lam et al. (2017). Our spectroscopic light curves were fitted with the planet radius–to–stellar radius ratio R_p/R_* as the sole free physical parameter, as well as fitting a slope and y-intercept for a wavelength-dependent systematic trend.

Following the procedure of H. R. Wakeford et al. (2020), we extracted transit depths $(R_p/R_*)^2$ at each wavelength from each order and averaged the results from the two orders together, excluding -1st-order wavelengths bluer than 250 nm because the -1st order mid-UV flux is too low for reliable analysis. We

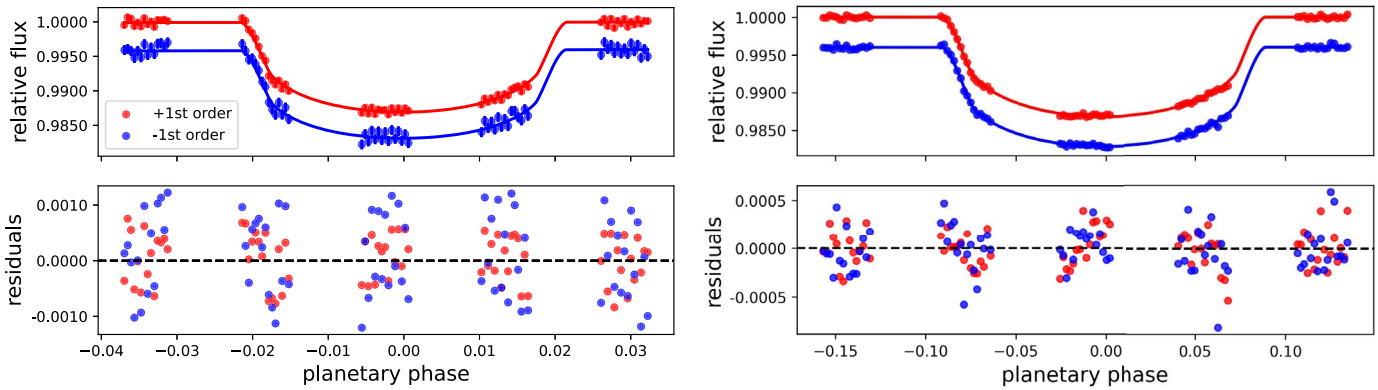

Figure 3. Top: normalized and detrended broadband light curves with fitted models overplotted. Bottom: residuals after fitting. The +1st-order light curves and residuals are in red, while blue denotes the −1st order. Left: the broadband light curves and residuals obtained by `hazelnut`. For clarity, a 400 ppm offset is applied to the −1st order. A "doubling" effect is seen in the light curves, most prominently in the −1st order. This effect arises from the method by which background values in each frame were selected; this doubling does not notably affect the results. Right: the broadband light curves obtained by `lluvia`. The broadband precision achieved by `lluvia` is greater; nevertheless, both pipelines obtain comparable median spectral precision and spectra largely consistent to 1σ.

additionally excluded the −1st-order wavelengths 397.5 nm and 407.5 nm, which, as stated in Section 2, suffered an unknown systematic that could not be removed by `ExoTiC-ISM`. We present our final `hazelnut` spectrum and limb-darkening coefficients in Appendix A, Table 5, as well as in Figure 4 alongside our `lluvia` reduction and spectra obtained by other observations. Our median spectroscopic precision in our 10 nm bins is ∼240 ppm.

To benchmark the performance of the WFC3/UVIS G280 grism in comparison to WFC3/IR and STIS gratings, we also rebinned our `hazelnut` 1D spectra to match the wavelength binning scheme used in J. J. Spake et al. (2021). To produce a near one-to-one comparison, we fit our rebinned light curves following the same limb-darkening model and system parameters as used by J. J. Spake et al. (2021). Our reduction, extraction, and fitting techniques are otherwise unchanged from the analysis detailed above; we present the results of this comparative analysis in Figure 4 and discuss its implications in Section 5.

3.2. `lluvia`

3.2.1. Systematics Removal

As with the light curves produced by `hazelnut`, the light curves produced by `lluvia` were also affected by HST systematics. We modeled each light curve $f(t)$ with a function of the form $f(t) = F_0 \times T(t, \theta) \times S(x)$, where F_0 is the baseline flux, $T(t, \theta)$ is the analytic transit model (which is a function of the system parameters θ) implemented through the `batman` package (L. Kreidberg 2015), and $S(x)$ is an instrument systematics model. Following the jitter decorrelation method described in D. K. Sing et al. (2019), we defined $S(x)$ as a linear combination of several detrending variables. These include optical state vectors estimated from the observations (e.g., HST orbital phase, displacements along the X and Y detector directions, etc.), and jitter vectors extracted from the HST Pointing Control System (e.g., telescope R.A., decl., etc.).

3.2.2. Broadband Light-curve Analysis

We also started by analyzing the broadband light curves, fitting for the midtransit epoch T_0, planet-to-star radius ratio R_p/R_*, and baseline flux F_0. However, we did not fit for system parameters a/R_* and b; instead, we fixed these values to those obtained by the `hazelnut` fit for consistency of comparison. Furthermore, we adopted the four-parameter nonlinear limb-darkening law as implemented in `ExoTiC-LD` (D. Grant & H. R. Wakeford 2024), using the 3D stellar models from Z. Magic et al. (2024), in contrast with our `hazelnut` fit, which uses a 1D stellar model grid. To avoid overfitting, we tested all the possible combinations of the detrending variables included in the instrument systematics model $S(x)$, and selected the subset of detrending variables that maximized the second-order Akaike Information Criterion (AIC_c). For all light curves, we first performed a linear least-squares fit of the $f(t)$ model to reject 3.5σ outliers and rescale the error bars to achieve a reduced-χ^2 of unity. We then refitted the $f(t)$ model through MCMC with `emcee` (D. Foreman-Mackey et al. 2013). We present the detrended and fitted broadband light curves in the right-side panels of Figure 3.

3.2.3. Spectroscopic Light-curve Analysis

We fitted each of the spectroscopic light curves following a similar procedure as in the broadband light-curve analysis, but fixing the midtransit epoch T_0 to the value extracted from the broadband light curves, and fitting only for the planet-to-star radius ratio R_p/R_* and the baseline flux F_0. Furthermore, we constructed our systematics model $S(x)$ using the best-fitting subset of detrending variables derived from the broadband analysis. We extracted two independent transmission spectra for orders +1 and −1, which we subsequently combined with a weighted mean to produce the final transmission spectrum. As in `hazelnut`, due to the poor precision in the bluer end of the −1st order, we excluded the −1st-order light curves below 250 nm. The final weighted spectrum is presented in panel 2 of Figure 4.

3.3. HST WFC3/UVIS G280 Spectrum

We present the UVIS spectra obtained by `hazelnut` and `lluvia` in Figure 4. We showcase the +1st and −1st orders separately for `hazelnut` (Figure 4, panel 1), and compare our `hazelnut` spectrum to our `lluvia` spectrum (Figure 4, panel 2) as well as to previous measurements of WASP-127b's spectrum (Figure 4, panel 3). We find that, while both UVIS/G280 pipelines were developed and operated mostly

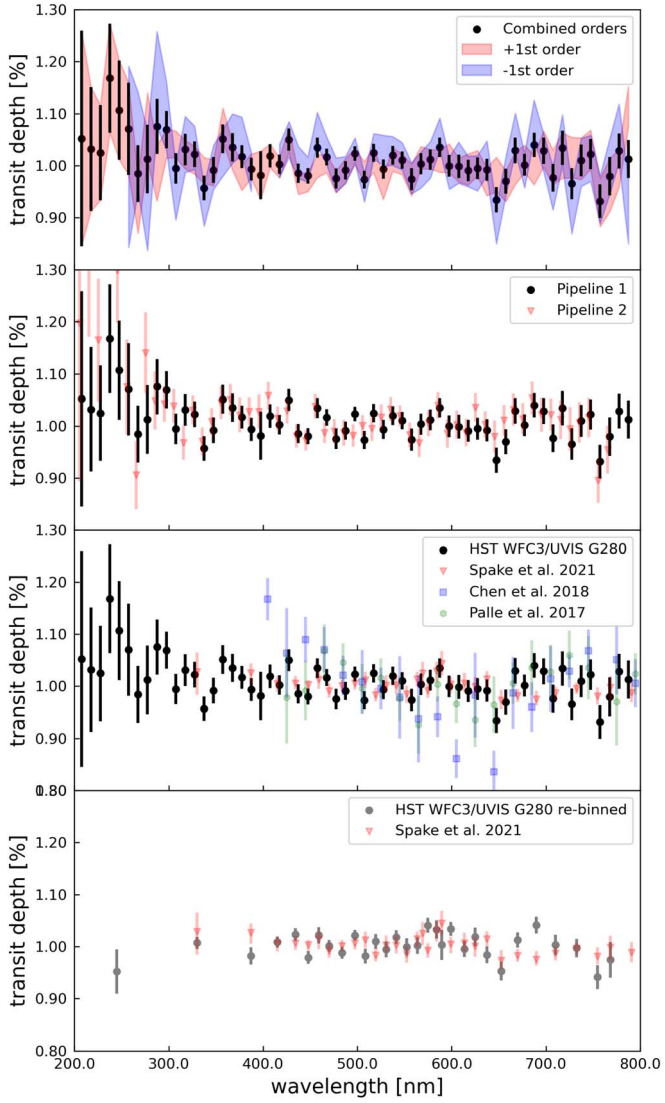

Figure 4. Spectra of WASP-127b obtained from this and other analyses. Panels are numbered 1–4 from the top. Panel 1: the `hazelnut` reduction of WASP-127b's HST WFC3/UVIS G280 observations shows the +1st and −1st orders both separately and combined. Transit depths below 250 nm and in between 397.5 and 402.5 nm from the −1st order are excluded for data-quality reasons. Panel 2: both reductions of our UVIS observations with no offsets applied, showing agreement to within 1σ for most points, with a steeper mid-UV spectrum obtained by the `lluvia` reduction that nonetheless remains within 1σ uncertainties. Panel 3: the `hazelnut` reduction compared to the spectra obtained by E. Palle et al. (2017), G. Chen et al. (2018), and J. J. Spake et al. (2021), with offsets of +236, −1050, and −222 ppm, respectively, applied to account for discrepancies arising from different detectors and observing epochs. Panel 4: the `hazelnut` spectrum rebinned to provide a near one-to-one comparison to J. J. Spake et al. (2021), with a −212 ppm offset applied to the latter spectrum.

independently and used different methods of cleaning and fitting the data, the majority of transit depths in both spectra agree to within 1σ. We also find our `hazelnut` spectrum with uniform 10 nm bins and independently determined system parameters to be in good agreement with the STIS spectra obtained by J. J. Spake et al. (2021), recovering a similar shallow slope as well as a small absorption peak near 670 nm corresponding to a well-known sodium absorption feature. The larger uncertainties in the spectra of E. Palle et al. (2017) and G. Chen et al. (2018) mean that both are consistent with our UVIS/G280 spectrum to within 1–2σ; however, the apparent strong slope in G. Chen et al. (2018) is not seen in either the STIS spectrum nor the UVIS/G280 spectrum. We discuss this further in Section 5. Our rebinned `hazelnut` spectrum (Figure 4, panel 4), which uses the same wavelength binning scheme, system parameters, and limb darkening as J. J. Spake et al. (2021), also shows reasonable agreement with J. J. Spake et al. (2021), with only a few notable discrepancies in the redder wavelengths and notably higher precision, which will also be discussed further in Section 5.

4. Forward Models and Atmospheric Retrievals

4.1. Forward Modeling with `PICASO` and `Virga`

Forward modeling was carried out on the primary reduction spectrum from `hazelnut` shown in Figure 4 and tabulated in Table 5. We utilized `PICASO` for both radiative transfer (N. E. Batalha et al. 2019) and self-consistent climate modeling (S. Mukherjee et al. 2023). `PICASO` is a radiative-convective thermochemical equilibrium (RCTE) model that allows the user to model the pressure–temperature (P-T) profile and 1D transmission or emission spectrum of an exoplanet or brown dwarf's atmosphere based on the object's temperature structure, gravity, and host-star characteristics.

`PICASO` self-consistently models equilibrium chemistry and clouds, the latter of which is made available by coupling `PICASO` to `Virga` (N. Batalha et al. 2020; C. M. Rooney et al. 2022), a program for modeling the distribution and composition of clouds in an exoplanet's atmosphere based on the methods of `eddysed` by A. S. Ackerman & M. S. Marley (2001). `Virga` provides a physically motivated estimate of the cloud contribution by including the wavelength-dependent opacity according to the particle size distribution. The aerosol size distribution is determined by the balance of cloud sedimentation efficiency ($f_{\rm sed}$) against upward vertical mixing as parameterized by the eddy diffusivity (K_{zz}) for condensing species.

By fitting a distribution of `PICASO` forward models to our WASP-127b transmission spectrum, inferences about the composition and structure of its atmosphere can be made. Our `PICASO` grid consists of atmospheric compositions set by the RCTE calculations of M. S. Marley et al. (2021) using correlated-ks of R. Lupu et al. (2021). These correlated-k opacities include C_2H_2, C_2H_4, C_2H_6, CH_4, CO, CO_2, CrH, Fe, FeH, H_2, H_3^+, H_2O, H_2S, HCN, LiCl, LiF, LiH, MgH, N_2, NH_3, OCS, PH_3, SiO, TiO, VO, Li, Na, K, Rb, and Cs. Our grid includes metallicities of 1×, 5×, 10×, 20×, 30×, 50×, and 100× solar and C/O ratios of 0.115, 0.229, 0.458, and 0.687, which correspond to 0.25×, 0.5×, 1×, and 1.5× solar C/O following K. Lodders (2010).

For the P-T profile, we initiate the profile with an initial estimate of the temperature structure from the parameterization of T. Guillot (2010), using an intrinsic temperature of 200 K (e.g., D. Thorngren et al. 2019) and a heat redistribution factor of 0.5. Previous works studying planets of a similar equilibrium temperature to WASP-127b (WASP-39b, WASP-17b; E.-M. Ahrer et al. 2023; L. Alderson et al. 2023; A. D. Feinstein et al. 2023; D. Grant et al. 2023; Z. Rustamkulov et al. 2023) have found negligible effects on cloud constraints by changing the intrinsic temperature within reasonable values (D. Thorngren et al. 2019) for a planet like WASP-127b. Our observations are also only sensitive to around 0.1 bar, and changing the intrinsic temperature would largely only change the pressure–temperature

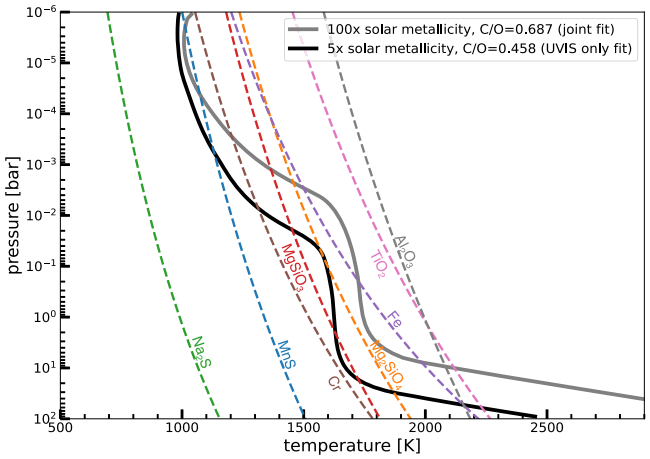

Figure 5. Pressure–temperature profiles computed by `PICASO 3.0` for WASP-127b, fitted with WFC3/UVIS G280 alone (black) and with the STIS G430L+G750L and WFC3/IR G141 spectra obtained by J. J. Spake et al. (2021; gray). Condensation curves at solar metallicity for typical cloud-forming species in hot Jupiter atmospheres (e.g., $MgSiO_3$, MnS) are also plotted; where the P-T profile crosses left of these curves, clouds of that condensate species may form.

profile deeper than a bar. After initializing our profile, we then iterate to locate the extent and placement of convective zones until convergence is reached. We inspect each computed cloud-free P-T profile for convergence before proceeding to post-processing clouds.

Using `Virga`, we added aerosol opacity accounting for clouds of MnS, $MgSiO_3$, and Mg_2SiO_4 with f_{sed} of 0.3, 0.6, 1, 3, and 6 and K_{zz} of 10^7, 10^9, 10^{11}, and 10^{13} $cm^2\,s^{-1}$. We account for atmospheric metallicity in our condensation of these cloud species. The range of metallicities we consider in our forward model grid produces varying pressure–temperature profiles and molecular abundances that also produce a wide range of potential cloud masses and locations to compare against our observations. In Figure 5 we present best fits of our `PICASO` P-T profiles, which are themselves cloud-free. We also show the condensation curves of cloud species shown under solar metallicity for illustration, demonstrating that the clouds we include in our `Virga` runs are possible to form in a variety of expected scenarios for WASP-127b. Though they are relevant given our temperature regime as shown in Figure 5, we do not include Fe or Cr clouds as it is expected to be difficult to nucleate and form such clouds compared to the silicate species (P. Gao et al. 2020). Furthermore, any Fe or Cr clouds that did form would do so at depth, below observable levels. While MnS is also expected to be sluggish to nucleate (P. Gao et al. 2020), the fact that its condensation curve crosses our temperature–pressure profiles at ∼millibar levels led us to include it in our model runs. SiO_2's condensation curve lies between $MgSiO_3$ and Mg_2SiO_4's (D. Grant et al. 2023), and so we do not model it separately as its contribution to our model spectra within Hubble's sensitivity is captured by the other two silicates.

To fit our `PICASO` forward models to the WFC3/UVIS G280 data, we generate synthetic transmission spectra from our converged climate profiles using `PICASO`'s radiative transfer module. For the radiative transfer, we use an opacity database containing the same species as above from 0.2 to 3 μm resampled to $R = 10{,}000$ from original line-by-line calculations at $R \sim 1 \times 10^6$ performed by R. S. Freedman et al. (2008) and E. Gharib-Nezhad et al. (2021). We bin the resulting models to the spacing of the data and compute a reduced-χ^2 to evaluate the goodness-of-fit. We consider three fits: (1) using the WFC3/UVIS G280 data of this work alone (59 degrees of freedom, DOF), (2) the J. J. Spake et al. (2021) HST data from STIS G430L+G750L and WFC3 G141 (61 DOF), and (3) a joint fit to the UVIS/G280 data combined with the HST/STIS G430L+G750L and HST/WFC3 G141 data (120 DOF). We allow for an offset of the J. J. Spake et al. (2021) combined HST reduction compared to our UVIS data. For our fit of the HST/STIS G430L+G750L and HST/WFC3 G141 data (61 DOF), we confirm that we recover a similar solution to that of J. J. Spake et al. (2021).

We show a selection of our forward model fits in Figure 6. Our clear model atmospheric spectra are all poor fits to the data, with a best-fit reduced-$\chi^2 = 2.3$ for the UVIS/G280 only fit (59 DOF), reduced-$\chi^2 = 24.7$ for the STIS G430L+G750L +WFC3 G141 fit (61 DOF), and reduced-$\chi^2 = 24.5$ (120 DOF) for the joint UVIS/STIS/G141 fit. Our cloudy fits comparatively provide reduced-$\chi^2 = 1.2$, 0.89, and 0.81, for UVIS, STIS/G141, and UVIS/STIS/G141, respectively. Our forward model grid tops out at 100× solar metallicity, which is expected to be a reasonable upper limit given the known constraints from JWST for a variety of giant planet atmospheres (E. M.-R. Kempton & H. A. Knutson 2024). Given this 100× solar metallicity limit, we are unable to generate clear atmospheres with small enough amplitudes at WFC3/G141 wavelengths to obtain good fits to the data, driving these large reduced-χ^2s for the clear runs. Conversely, adding cloud opacity easily suppresses the amplitude of the water feature present in WFC3/G141, resulting in the much better reduced-χ^2s for the cloudy models.

The clear atmosphere preferred models are all uniformly 100× solar metallicity, while cloudy models reduce the best-fit preferred metallicity down to 1× solar for the UVIS/G280 data alone, 100× solar for the STIS/G141 data alone, and 50× solar for the joint fit. However, this is not strongly constrained by our `PICASO` forward models, and the degeneracy between metallicity and cloud parameters means that any number of combinations provide a good fit to the data. For example, we find that our goodness-of-fits for the joint data set (G280+STIS +G141; 120 DOF) range from 5 to 100× solar metallicity across the full range of cloud parameters with reduced-χ^2 from 0.8 to 2.0, which is not a statistically significant interval. Nonetheless, the significant difference in fits between our clear and cloudy runs suggests that stronger scattering imparted by aerosol particles, combined with the muting of the water feature in the WFC3/G141 bandpass, requires the presence of clouds in our forward models.

Within our modeling framework, f_{sed} parameterizes the efficiency with which particles sediment down through the atmosphere while K_{zz} sets the strength of upward vertical mixing. Therefore, the balance between K_{zz} and f_{sed} sets cloud particle sizes, with larger cloud particles in more compact layers produced by large f_{sed} and small K_{zz}, or smaller cloud particles in more extended cloud layers produced by small f_{sed} and larger K_{zz}. Our best-fitting cloudy models range $K_{zz} = 10^9$–10^{11} $cm^2\,s^{-1}$ with $f_{sed} \leqslant 1$. The UVIS/G280 only fits have an $f_{sed} = 0.6$, while the STIS/G141 and joint fits have a wider spread anywhere in the range $f_{sed} = 0.3$–1. For the UVIS/G280 cloudy fits, our `Virga` runs result in micron-sized

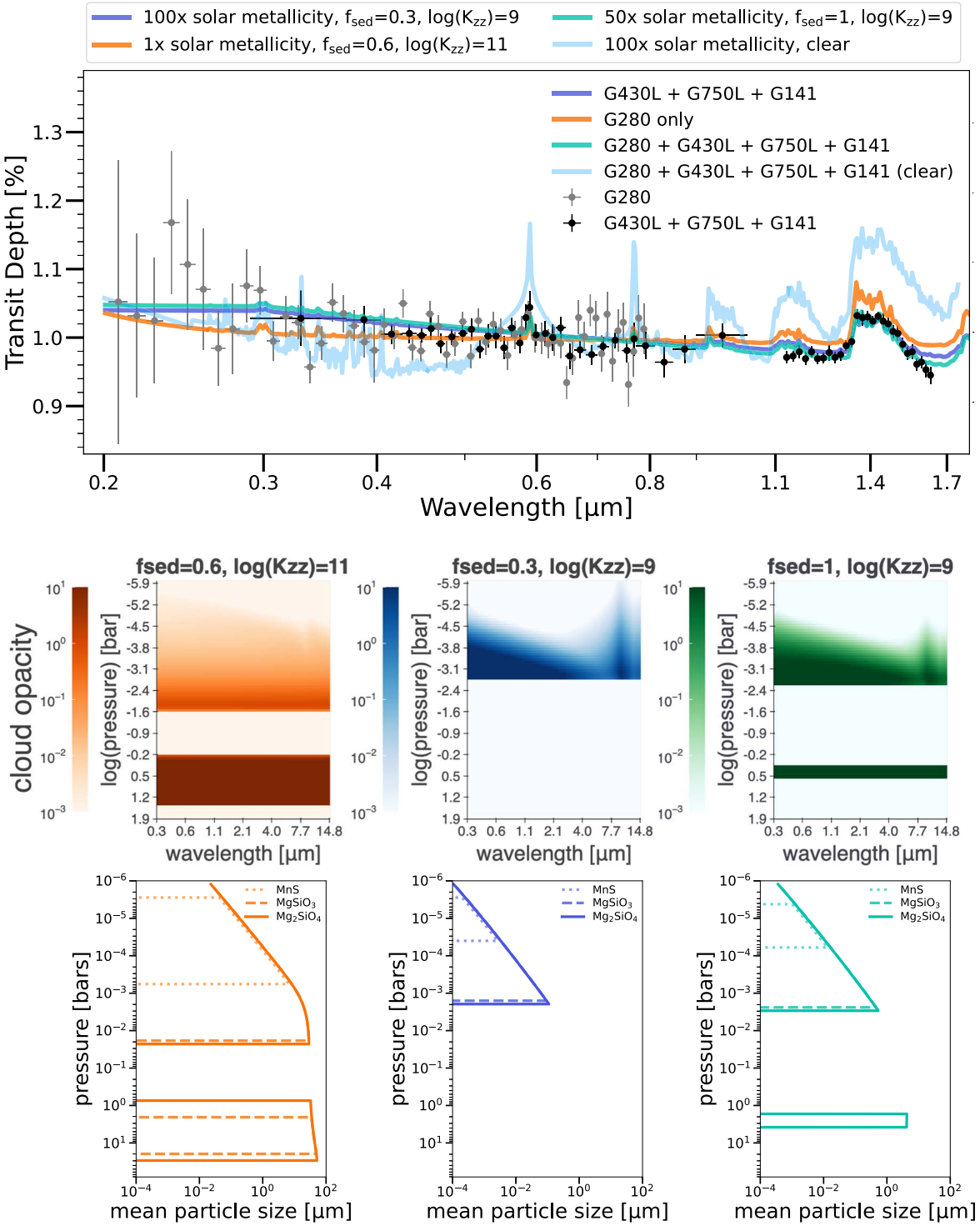

Figure 6. Top: PICASO best-fit forward models of the UVIS/G280 spectrum of WASP-127b (gray points), fitted both separately and jointly with the STIS G430L +G750L and WFC3/IR G141 spectra obtained by J. J. Spake et al. (2021; black points). The best fit of a clear jointly fitted model is also shown in light blue, demonstrating that clouds are required to fit the spectrum well. Middle: cloud opacities for the single best-fitting Virga runs for the UVIS/G280 spectrum (orange), STIS/G141 spectrum (blue), and joint fit (green). Bottom: mean particle sizes for each corresponding Virga run in the row above.

particles made primarily of silicates, while the STIS/G141 data alone favor cloudy fits with submicron-sized particles.

None of the cloud mixing parameters have particularly strong constraints, but when analyzed jointly, the data result in cloudy models with relatively high-altitude (∼millibar–microbar), small (submicron) cloud particles. All the cloud fits result in a cloud layer dominated by silicate opacity, with only a very optically thin contribution from any MnS cloud. We examined whether MnS clouds alone could match the data, and found that their much smaller cloud mass and correspondingly weaker opacity means that silicate clouds are required to explain the data given our model setup. The cloud scenario for each data set combination is shown in the lower two rows of Figure 6, which highlights both the cloud optical depth (middle row) and

the mean effective particle size in the cloud layer by species (bottom row), demonstrating the dominance of silicate cloud compared to manganese sulfide cloud opacity.

4.2. Retrievals with POSEIDON

We additionally perform an atmospheric retrieval analysis, in which the parameter space of possible spectra is built by varying different model parameters (e.g., molecular abundances, P-T profiles, and aerosol properties). Retrievals employ Bayesian methods to explore the model parameter space and determine the range of atmospheric properties that provide good fits to the data. For our retrievals, we employ the open source POSEIDON code (R. J. MacDonald & N. Madhusudhan 2017; R. J. MacDonald 2023).

4.2.1. Retrieval Configuration

We construct a suite of retrievals to assess the contribution of our UVIS/G280 observations to the inferred atmospheric parameters of WASP-127b. Our retrievals consider multiple combinations of data sets, including G280 alone, G280 in concert with archival WASP-127b transmission spectra from J. J. Spake et al. (2021; STIS, WFC3/IR G141, and Spitzer photometry), and the archival data alone.

Our retrievals employ a parametric model of a H_2–He dominated atmosphere containing multiple trace chemical species. We assume 1D atmospheres (varying only with altitude) with an isothermal P-T profile, parameterized by the isothermal temperature, T, and a pressure grid with 100 levels spanning 100–10^{-9} bar. We parameterize trace chemical species via their $\log_{10}$ volume mixing ratio (VMR), considering atomic and molecular opacities from Na (T. Ryabchikova et al. 2015), K (T. Ryabchikova et al. 2015), FeH (S. Wende et al. 2010), H_2O (O. L. Polyansky et al. 2018), CH_4 (S. N. Yurchenko et al. 2017), CO (G. Li et al. 2015), and CO_2 (S. A. Tashkun & V. I. Perevalov 2011). H_2 and He pressure broadening is applied for all species except FeH (which uses the broadening prescription from C. M. Sharp & A. Burrows 2007). Our retrievals also consider inhomogeneous aerosols via the four-parameter prescription from R. J. MacDonald & N. Madhusudhan (2017). This parameterization couples optical scattering (defined by two parameters: the power-law exponent of the scattering slope, γ, and an enhancement over Rayleigh scattering, $\log a$) with an opaque gray cloud deck, defined at a cloud top pressure $\log(P_{\rm cloud})$, covering a fraction $\phi_{\rm cloud}$ of the terminator. For retrievals with multiple data sets, we include a free offset, $\delta_{\rm rel}$, between the UVIS G280 data and the archival data. STIS, WFC3, and Spitzer were not offset from each other in this analysis as they were jointly analyzed by J. J. Spake et al. (2021), who included offsets in their own work. G280 as a separate analysis required the consideration of an offset to the prior jointly analyzed data. We additionally fit for the radius of the planet at the 10 bar reference level, $R_{p,\rm ref}$. We compute model spectra for each atmosphere on a wavelength grid with $R = 5000$ from 0.18–5.2 μm. Our retrievals have a maximum of 14 free parameters, with the parameters and priors summarized in Table 2. We evaluate the parameter space using PyMultiNest (F. Feroz & M. P. Hobson 2008; J. Buchner et al. 2014) with 4000 live points for each nested sampling run.

We initially ran retrievals on the G280 data alone, using our base retrieval configuration and models with Na and FeH excluded. These latter two retrievals allow Bayesian model comparisons to assess the statistical evidence for Na and FeH. We focus on Na and FeH as these are the only chemical species with significant absorption features over the UVIS/G280 wavelength range that improve the Bayesian evidence for some model and data combinations. We also conducted the same model comparisons for retrievals combining the G280, Spitzer, and subsets of the HST IR observations (G141 and/or STIS). We further consider the influence of a fixed offset between the G280 and IR data (adopting an offset of 195 ppm for G280). Finally, for comparison with J. J. Spake et al. (2021), we also include a retrieval without our G280 data (only G141, STIS, and Spitzer). Our full suite of retrieval models is summarized in Table 3. We also report in Table 4 statistical metrics for the goodness-of-fit for all our retrieval models, including the log Bayesian evidence, $\ln \mathcal{Z}$, the Bayesian Information Criterion (BIC), the reduced chi-squared, χ^2_ν, the χ^2 cumulative distribution function (CDF; T. J. Wilson 2021), Bayes factors, $\mathcal{B}$, and chemical species detection significances.

Table 2
Retrieval Free Parameters and Priors

Parameter	Prior Distribution	Prior Range
$R_{p,\rm ref}$ ($R_{\rm p}$)	uniform	0.85 to 1.15
T (K)	uniform	400 to 2300
$\log X$	uniform	−12 to −1
$\log a$	uniform	−4 to 8
γ	uniform	−20 to 2
$\log P_{\rm cloud}$	uniform	−7 to 2
$\phi_{\rm cloud}$	uniform	0 to 1
$\delta_{\rm rel}$ (ppm)	uniform	−1000 to 1000

Note. The reference radius, $R_{p,\rm ref}$, defined at a pressure of 10 bar, spans a prior ranging from 85% to 115% of the white-light radius of WASP-127b (1.311 R_J). The relative offset $\delta_{\rm rel}$ is measured in parts per million.

4.2.2. Retrieval Results

Our initial retrievals using only the UVIS/G280 data set resulted in a nondetection of a scattering slope or any significant chemical absorption features. Since the UVIS data alone are essentially featureless, the retrieved temperature has only a 2σ upper limit of 849 K. We therefore focus our subsequent retrieval investigations on joint retrievals between the UVIS/G280 data and the archival HST and Spitzer data from J. J. Spake et al. (2021) to better constrain WASP-127b's atmospheric properties. We report the median atmospheric parameter values and 1σ confidence intervals for our suite of retrievals in Table 6, presented in Appendix B.

Our strongest constraints on WASP-127b's atmosphere arise from jointly retrieving our UVIS/G280 data, alongside HST/STIS, HST/G141, and Spitzer photometry. The best-fitting model (model F) results in bounded constraints on H_2O ($-3.91^{+0.18}_{-0.17}$ dex), CO_2 ($-4.82^{+0.37}_{-0.42}$ dex), Na ($-7.21^{+0.34}_{-0.39}$ dex), and FeH ($-8.29^{-0.56}_{-1.07}$ dex). We detect Na at 4.1σ but find only marginal evidence of FeH (2.0σ). These values are similar to those presented in G. Chen et al. (2018) and J. J. Spake et al. (2021), respectively. We do not detect K, CH_4, or CO. We show the retrieved transmission spectrum and posterior distributions from this model in Figure 7 (turquoise). Our H_2O and CO_2 constraints imply a slightly subsolar (0.2× −0.5×) metallicity from H_2O and a slightly supersolar (15× to 100×) metallicity from CO_2, assuming a solar C/O ratio. These values are in agreement with

Table 3
POSEIDON Retrievals Applied to WASP-127b's Transmission Spectrum

Model + Data Combination	Chemical Species	G280 Offset
G280		
Model A	Na + K + H_2O	...
Model B	K + H_2O	...
Model C	Na + K + H_2O + FeH	...
G280 + G141 + STIS + Spitzer		
Model D	Na + K + H_2O + CO + CH_4 + CO_2	V
Model E	K + H_2O + CO + CH_4 + CO_2	V
Model F	Na + K + H_2O + CO + CH_4 + CO_2 + FeH	V
G280 + G141 + Spitzer		
Model G	Na + K + H_2O + CO + CH_4 + CO_2	V
Model H	K + H_2O + CO + CH_4 + CO_2	V
Model I	Na + K + H_2O + CO + CH_4 + CO_2 + FeH	V
Model J	Na + K + H_2O + CO + CH_4 + CO_2	F (195 ppm)
Model K	K + H_2O + CO + CH_4 + CO_2	F (195 ppm)
Model L	Na + K + H_2O + CO + CH_4 + CO_2 + FeH	F (195 ppm)
G141 + STIS + Spitzer		
Model M	Na + K + H_2O + CO + CH_4 + CO_2 + FeH	...

Note. "STIS" refers to the combination of G430L and G750L observations. All models contain additional parameters for cloud opacity ($\log a$, γ, $\log P_{\rm cloud}$, and $\phi_{\rm cloud}$) and an isothermal temperature profile. Retrievals where the UVIS/G280 data have a free offset are denoted by a "V" (Variable offset). Retrievals where the offset is fixed to the median retrieved value from model D (195 ppm) are denoted with an "F" (Fixed).

Table 4
Bayesian Model Comparisons and Model-fit Statistics

Model	DOF	$\ln \mathcal{Z}$	BIC	χ^2_ν	χ^2 CDF (%)	$\mathcal{B}$	Detection Significance
A	50	384.15	104.19	1.35	95.00	...	...
B	51	384.18	101.47	1.35	95.15	0.97	[Na] Nondetection
C	49	384.27	107.91	1.37	95.64	1.13	[FeH] Nondetection
D	111	858.59	203.63	1.27	97.12	...	...
E	112	851.85	216.88	1.42	99.77	846	[Na] 4.1σ
F	110	859.54	204.98	1.25	96.10	2.49	[FeH] 2.0σ
G	76	604.99	163.23	1.38	98.42	...	...
H	77	604.74	160.12	1.38	98.48	1.28	[Na] 1.4σ
I	75	606.15	162.59	1.33	97.04	3.19	[FeH] 2.1σ
J	77	604.60	156.27	1.33	97.19	...	...
K	78	603.67	153.90	1.34	97.58	2.53	[Na] 2.0σ
L	76	604.86	160.19	1.34	97.44	1.30	[FeH] 1.4σ
M	53	473.44	114.22	1.21	85.93	...	...

Note. "DOF" is the number of degrees of freedom ($N_{\rm data} - N_{\rm params}$), $\mathcal{Z}$ is the Bayesian evidence, "BIC" is the Bayesian Information Criterion, χ^2_ν is the reduced chi-squared, χ^2 CDF is the chi-squared cumulative distribution function, and $\mathcal{B}$ is the Bayes factor between a model including Na (Models B, E, H, and K) or FeH (Models C, F, I, and L) and a nested model without Na or FeH.

the retrievals performed in J. J. Spake et al. (2021), as well as abundances derived for similar-temperature planets (e.g., D. Grant et al. 2023). Further infrared data as would be possible from JWST are needed to constrain the full inventory of oxygen- and carbon-bearing species and thus the atmospheric metallicity.

We investigated the robustness of the Na detection via additional retrievals with subsets of the data. In removing the G280 data (Model M), we see the Na abundance and constraints remain consistent (Figure 7, blue distributions). By instead removing the STIS data and using a fixed G280 offset (model L), the retrieved Na abundance remains in agreement with model F, although the abundance constraint is weaker. When G280 is the only optical data, we find a reduced detection significance for Na (2.0σ with a fixed offset, 1.4σ with a variable offset between the G280 and IR data). We note that C. Fairman et al. (2024) found a similar Na detection significance of 2.9σ from a POSEIDON retrieval on the HST/STIS+G141+Spitzer data (but without FeH opacity).

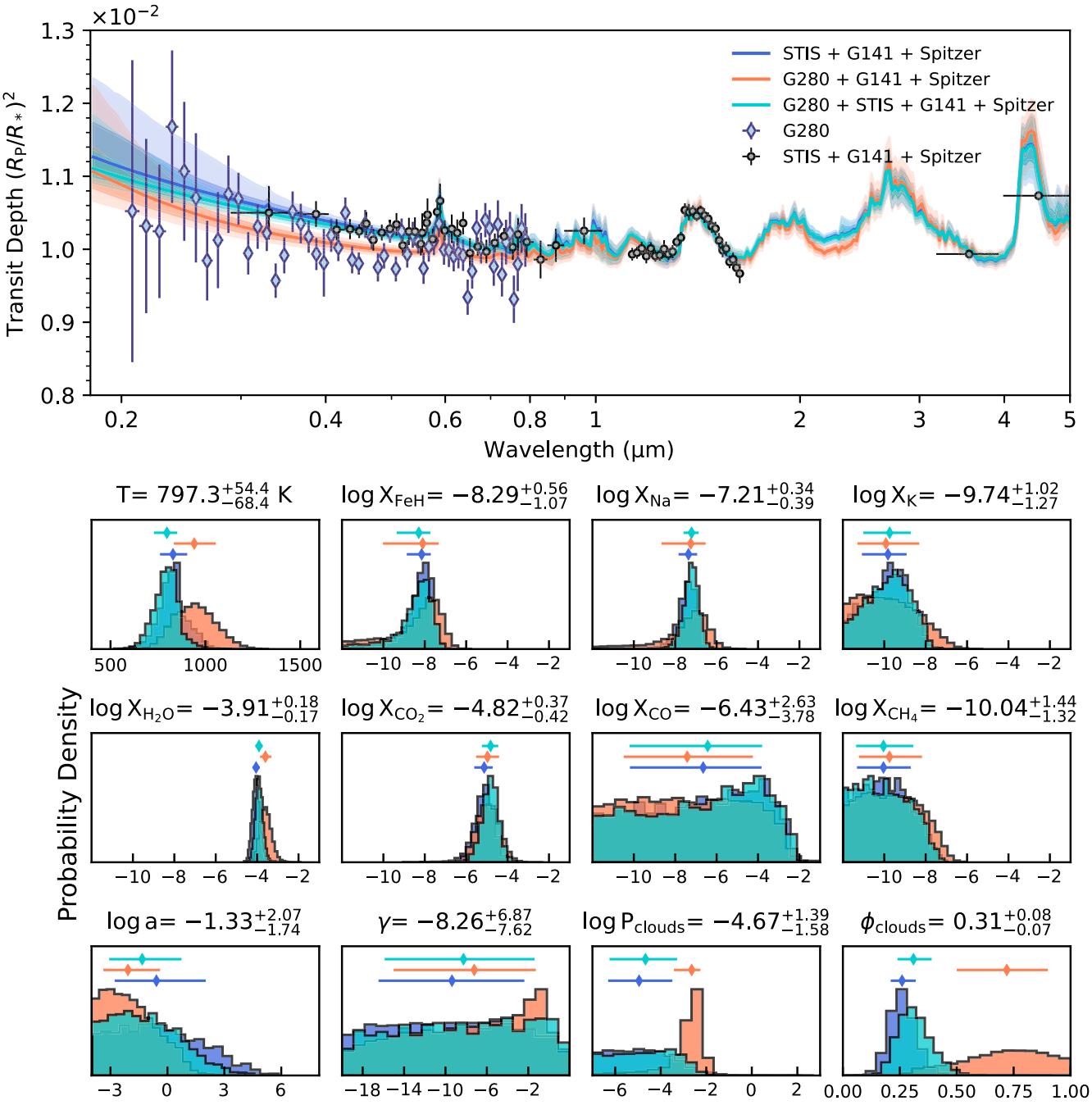

Figure 7. Retrieved POSEIDON transmission spectra and posterior distributions of WASP-127b. Top: retrieved transmission spectra for three data set combinations: (1) the combined data set from G280 + STIS + WFC3/G141 + Spitzer (model F, turquoise); (2) G280 + WFC3/G141 + Spitzer (model L, orange); and (3) STIS + WFC3/G141 + Spitzer (model M, blue). We note that Model F allows for a variable offset between the UVIS/G280 and J. J. Spake et al. (2021) data (STIS + WFC3/G141 + Spitzer), where a median G280 offset of 195 ppm is found. This offset is applied as a fixed value for model L between the UVIS/G280 and IR data. Shaded regions mark the 1σ and 2σ confidence intervals, and error bars give the retrieved median parameter values and their respective 1σ errors. Retrieved median values and 1σ errors are presented for model F.

Therefore, although neither the STIS nor UVIS/G280 data can confidently detect Na independently, their combined information provides a stronger detection (4.1σ).

The inferred FeH abundance from our retrievals ($\log\mathrm{FeH} = -8.29^{+0.56}_{-1.07}$) is potentially consistent with expectations from chemical models. Equilibrium chemistry predicts FeH mixing ratios between 10^{-10} and 10^{-8} dex in exoplanet atmospheres with equilibrium temperatures >1000 K at deep pressures of 1 bar up to millibar pressures (P. Woitke et al. 2018). The FeH abundance drops off significantly with altitude due to the probable sequestration of Fe into clouds (C. Visscher et al. 2010). Our best-fit cloudy and cloud-free PICASO+Virga forward models and the retrieved values from POSEIDON agree on the FeH abundance for WASP-127b to within 1σ. Vertical mixing may contribute to the observed abundance of FeH in WASP-127b's atmosphere, but is not required given current abundance constraints. Evidence of metal hydrides has been reported in giant exoplanet atmospheres across a range of equilibrium temperatures (e.g., T. M. Evans et al. 2018; R. J. MacDonald &

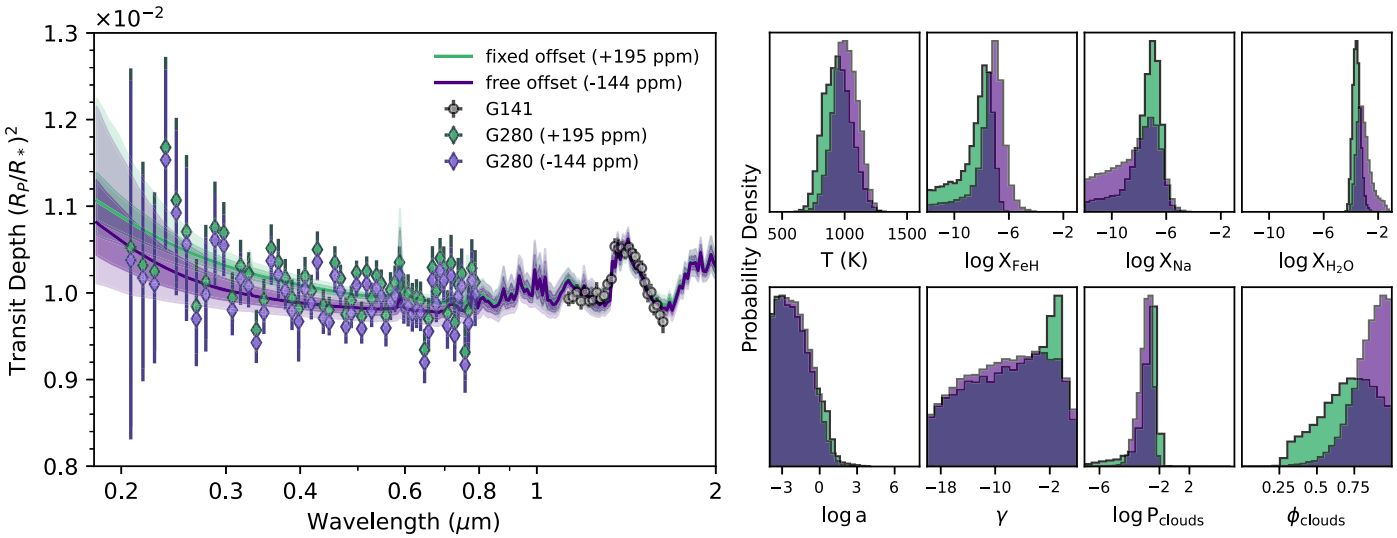

Figure 8. A comparison of the retrieved spectra and selected posterior distributions in allowing a fixed offset at +195 ppm (model L, green) to a variable offset (model I, purple) between the UVIS/G280 and IR (WFC3/G141 + Spitzer) data sets. Shaded regions mark the 1σ and 2σ confidence intervals

N. Madhusudhan 2019; N. Skaf et al. 2020; K. S. Sotzen et al. 2020; L. Flagg et al. 2023), including for WASP-127b (N. Skaf et al. 2020; J. J. Spake et al. 2021). N. Skaf et al. (2020) report from WFC3/IR G141 data alone a higher abundance of FeH (logFeH ~ -5), while J. J. Spake et al. (2021) find from G141 + STIS + Spitzer data a consistent FeH abundance with our results (logFeH ~ -7.5). We stress that the highest FeH detection significance we find is only 2.1σ (Model I). Therefore, we conclude that our new G280 data do not provide any additional evidence for FeH in WASP-127b's atmosphere, with the weak inference for FeH driven instead by the WFC3/IR G141 data.

Our retrievals favor the presence of an optically thick high-altitude cloud deck. Using the combined data (Model F: G280 + STIS + G141 + Spitzer), we find high-altitude patchy clouds with a terminator coverage fraction of $0.31^{+0.08}_{-0.07}$. When fitting for a homogeneous cloud coverage, the probability distribution for the reference radius becomes low, tending toward the lower end of the prior range. This in turn results in an unrealistically tight constraint on gamma, which would represent no enhancement over Rayleigh scattering. When allowing for patchy cloud coverage, the reference radius value recovers a Gaussian distribution and we find gamma to be unconstrained at $-8.24^{+6.93}_{-7.58}$, which is more representative of our observational uncertainties where scattering is dominant in the atmosphere (<0.5 μm). However, the inference of patchy clouds depends crucially on the STIS data (0.3–0.9 μm), where a patchy cloud opacity is needed to fit both the flat spectrum and the more prominent Na feature. When we remove the STIS data and retrieve only the G280 and IR data with a fixed offset (model L), the model lies more centrally through the scatter in the G280 data. This lowers and flattens the model transit depths between 0.4 and 0.8 μm, resulting in a uniform cloud fraction with a median retrieved cloud pressure deeper in the atmosphere ($\log P_{\rm cloud} \sim 10^{-2.5}$ bar). Without the STIS data, the retrieved median temperature and H_2O abundance increases to compensate for the change from patchy to uniform clouds (see Figure 7). These changes are small within the uncertainties of the retrieved parameters, demonstrating that the inferred atmospheric composition of WASP-127b is robust to these permutations of the included optical data. Finally, we show in Figure 8 that considering a variable G280 offset instead of a fixed offset (Model I versus Model L) increases the preference for uniform terminator cloud coverage.

Contrasting with our inference of clouds, we find a nondetection of scattering hazes. This is shown in the posterior distributions in Figure 7 by the scattering slope parameter, γ, being unconstrained, and $\log a$ having only an upper limit. The nondetection of hazes arises from the small slope at optical wavelengths, which can be explained solely from the contribution of H_2 Rayleigh scattering from the clear terminator sector in the patchy cloud model. We find the same absence of aerosol scattering when the G280 data are absent (see Figure 7), as the relatively flat UVIS/G280 spectrum is consistent with the STIS observations. We note that our G280 data are inconsistent with the sharp rise in optical transit depths seen in the ground-based observations of WASP-127b in E. Palle et al. (2017) and G. Chen et al. (2018). Therefore, our retrievals indicate an optically thick cloud deck but a lack of small scattering aerosols in WASP-127b's atmosphere.

5. Discussion

5.1. Interpretation of WASP-127b's G280 Spectrum

We presented `PICASO` forward models and `POSEIDON` retrievals in Section 4 that combined UVIS/G280 observations with previous optical and IR spectra. Both interpretation methods suggest an atmosphere with at least partial cloud cover. The forward model suggests a denser cloud deck below millibar levels and a second, more diffuse cloud deck that extends from around a millibar up to around a microbar; the retrieval supports evidence for patchy clouds.

Theory predicts that at $T_{\rm eq} \sim 1400$ K silicate clouds begin to sink from the observable atmosphere and can be found only at high pressure layers deep in the atmosphere, if they are found at all, while manganese sulfide clouds begin to condense in the upper atmosphere (e.g., C. Visscher et al. 2010; V. Parmentier et al. 2016). This is roughly in line with the results of our `PICASO+Virga` models, where we observe that the millibar–microbar cloud layer is composed of minor amounts of manganese sulfide clouds along with silicate clouds. The deep, denser cloud deck is entirely silicate. Future studies should pursue these claims with JWST MIRI, which can resolve

absorption features unique to silicate species (e.g., D. Grant et al. 2023), though MnS lacks distinctive mid-infrared absorption (H. R. Wakeford & D. K. Sing 2015). Our best-fit `Virga` models, in particular, suggest strong silicate opacity for WASP-127b (middle panel, Figure 6), which JWST MIRI could observe. Moreover, SiO_2 clouds could also contribute to the silicate cloud layer (e.g., D. Grant et al. 2023), and MIRI observations could determine the specific identity of silicate clouds, which is beyond the capability of Hubble.

SNR limits the ability of the added G280 data to strongly constrain cloud properties via the scattering gradient and Rayleigh enhancement factor from `POSEIDON` or mixing and sedimentation parameters from `Virga`. Nonetheless, the UVIS/G280 spectrum is consistent with a shallow slope and the overall flatness of the spectrum suggests a Rayleigh scattering haze flattened by patchy cloud cover. Small particle sizes under 1 μm are favored by the UVIS/G280 spectrum combined with the STIS and G141 data. Weak evidence for sodium is retrieved, but no evidence is found for potassium or lithium, consistent with previous optical and IR studies of WASP-127b with HST (J. J. Spake et al. 2021). While the overall spectrum shape is flat or slightly inclined, modest evidence of H_2O and CO_2 absorption is recovered, as is weak evidence of sodium absorption, consistent with partial cloud coverage that mutes, but does not fully suppress, all absorption features.

Our UVIS/G280 data can provide only upper bounds on the amount of CH_4 and CO, as to be expected since neither species has any strong absorption features in the UVIS/G280 wavelength range; JWST observations should be carried out to constrain the CH_4 abundance and break the CO/CO_2 degeneracy for WASP-127b.

5.2. Direct Comparison to HST WFC3/IR and STIS Spectroscopy

As WASP-127b has been studied with HST spectroscopy before, our work provides an important benchmark of the performance of the UVIS/G280 as compared to other HST instruments. We carried out an extraction emulating the work of J. J. Spake et al. (2021), benchmarking the observing potential of the underutilized UVIS/G280 against the more standard STIS G430L+G750L combination used by other studies. The UVIS/G280 throughput in the near- to mid-UV ranges from around 10% to 30%, considerably higher than the <5% throughput of the STIS G430L in the near-UV. J. J. Spake et al. (2021) utilized the STIS G430L and achieved a precision of about 400 ppm in a spectral bin spanning 289.8–370.0 nm; in this same wavelength bin and following identical fitting procedures, our UVIS/G280 observations achieved a precision of 66 ppm, a factor of 6 times more precise than what the STIS G430L achieved. However, we note the UVIS/G280 spectrum extracted here shows notably more scatter than that obtained by STIS; data points in the STIS spectrum lie closer to a smooth line, while the UVIS/G280 spectrum shows a notable "zigzag" pattern. Unusual sky background values have been observed in other UVIS/G280 transmission observations (H. R. Wakeford et al. 2020) and are believed to be a UVIS/G280-specific systematic signal that is not yet understood; the zigzag seen here likely originates from the same unusual background behavior. Removal of this suspected systematic is expected to remove the zigzag pattern without significantly changing the results of this work. The superior throughput of the UVIS/G280 in near-UV wavelengths thus has the potential to place stronger constraints of a hot Jupiter's UV spectrum than can be achieved with STIS grisms, and further work should be carried out to better characterize and treat its instrument systematics to unlock its full potential.

5.3. Other Studies of WASP-127b

Our HST UVIS/G280 spectrum, like the HST STIS and IR spectra presented in J. J. Spake et al. (2021), shows no evidence of lithium or potassium. Previous studies using ground-based instruments reported detections of lithium and potassium to 3.4σ and 5.0σ, respectively (G. Chen et al. 2018). Telluric O_2 absorption features can complicate ground-based observations of exoplanetary potassium (e.g., N. P. Gibson et al. 2017); we therefore suspect that previous observations of lithium and potassium may instead be telluric contamination. Our forward models favor submicron particle sizes as were favored by G. Chen et al. (2018); however, with the increased precision achievable with HST, we find stronger evidence for a sub-Rayleigh scattering and shallow gradient, consistent with the sub-Rayleigh slope found by J. J. Spake et al. (2021). As stated in Section 3, the larger uncertainties in the spectra of E. Palle et al. (2017) and G. Chen et al. (2018) are consistent with our results, even as the previously reported super-Rayleigh slope has disappeared.

Recent ground-based high-resolution cross-correlation studies have also detected H_2O (A. Boucher et al. 2023) and both H_2O and CO in WASP-127b (K. Kanumalla et al. 2024; L. Nortmann et al. 2024). Observations with these high-resolution spectrographs have resulted in contradictory interpretations of the carbon content and metallicity of WASP-127b's atmosphere. The Spectro-Polarimètre InfraRouge (SPIRou) spectrograph on the Canada–France–Hawaii telescope found subsolar C/O and only upper limits of CO (A. Boucher et al. 2023), while observations with the Immersion Grating Infrared Spectrometer (IGRINS) on Gemini South and the Cryogenic Infrared Echelle Spectrograph (CRIRES$^+$) of the European Southern Observatory both have higher SNR and were able to recover CO constraints for the planet (K. Kanumalla et al. 2024; L. Nortmann et al. 2024), indicating subsolar-to-solar C/O.

Similarly, the metallicity constraints enabled by these high-resolution cross-correlation studies vary from solar (L. Nortmann et al. 2024) to significantly metal-rich ($\sim$40$\times$ solar; A. Boucher et al. 2023; K. Kanumalla et al. 2024). These varied interpretations are in line with our retrievals on the combined G280 + STIS + G141 + Spitzer data, where both our study and the cross-correlation interpretations rely on the Spitzer photometry for contributions from CO_2 as the most powerful tracer of atmospheric metallicity. Both L. Nortmann et al. (2024) and A. Boucher et al. (2023) find H_2O abundances in agreement to 1σ with those we detect here, while K. Kanumalla et al. (2024) retrieve a H_2O VMR 2 orders of magnitude higher than our 1σ bound.

These high-resolution cross-correlation (HRCC) studies all also find evidence for a substantial gray cloud deck that ranges from tens of millibars (A. Boucher et al. 2023) to 1–0.1 millibar (K. Kanumalla et al. 2024; L. Nortmann et al. 2024), in agreement with our space-based data interpretation. Interestingly, the three cross-correlation studies also all find evidence of significant blueshifted (A. Boucher et al. 2023;

K. Kanumalla et al. 2024; L. Nortmann et al. 2024) and redshifted (L. Nortmann et al. 2024) signal peaks, indicative of a supersonic equatorial jet and significant day-night temperature contrasts. This inferred atmospheric profile from HRCC, combined with our cloud parameter constraints, strongly supports JWST follow-up studies of this intriguing world to better understand its temperature structure, chemistry, and clouds.

6. Conclusions

We present the UVIS transmission spectrum of WASP-127b taken through the HST WFC3/UVIS G280 as part of the HUSTLE program. Our primary spectrum spans 200 nm to 800 nm, achieving a broadband precision of 91 ppm and a median precision of ∼240 ppm in 10 nm wide bins. A supplementary reduction using an independent pipeline was statistically consistent with the results of our primary reduction, supporting the claim by H. R. Wakeford et al. (2020) that G280 observations are consistent enough to provide meaningful results independent of particular reduction and analysis techniques.

Forward models show a strong preference for the presence of clouds, and while not strongly constrained all models favor clouds of submicron particles at relatively high altitudes. Attempts to fit clear atmospheric models to the data with forward modeling yield fits of poor quality requiring very supersolar metallicities, disfavoring the clear sky interpretation of WASP-127b's transmission spectrum. Retrievals recover modest evidence for Na absorption with an overall detection confidence of 4.1σ when G280 is combined with archival space-based transmission spectra. Any observed signature of Na absorption suggests that the cloud coverage cannot be total. Our retrievals favor a partial cloud coverage fraction of $\phi \sim 0.31$. Evidence for FeH, previously inferred from G141 data by N. Skaf et al. (2020; 4.0σ) and J. J. Spake et al. (2021; 2.0σ), is not strengthened with the inclusion of G280 data.

Extending the spectral coverage down to mid-UV wavelengths shows that the scattering slope, while weakly constrained here, is sub-Rayleigh in nature, consistent with claims by J. J. Spake et al. (2021) and contradictory to results obtained from the ground (E. Palle et al. 2017; G. Chen et al. 2018). The small slope can be accounted for with H_2 Rayleigh scattering from the clear component of the terminator, with an opaque cloud deck elsewhere. The equilibrium temperature of WASP-127b is in the correct range to be at a transition point in aerosols where silicate clouds subside and manganese sulfide clouds begin to condense in the upper atmosphere (e.g., V. Parmentier et al. 2016). We recommend future studies of WASP-127b to complement this work through JWST observations in the near- and mid-IR, where absorption signatures from silicates can be detected, confirming the partial clouds found here and constraining their composition.

Our study demonstrates the potential for the UVIS/G280 to be a more efficient observing mode for UVIS spectroscopy than what is typically achieved using HST STIS. In comparison to previous studies of WASP-127b through STIS observing modes (J. J. Spake et al. 2021), our UVIS/G280 observations achieve a near-UV (289.8–370.0 nm) precision of 66 ppm, about 6 × greater precision than was achieved by the standard STIS G430L+G750L observing mode combination, albeit with higher scatter for which we recommend further study of the instrument's systematics to resolve. We achieve this precision in just one transit observation in comparison the two-transit minimum that is imposed by STIS spectroscopy. The HST WFC3/UVIS G280's spectral range of 200–800 nm provides a much deeper probe into the UV than can be achieved with STIS G430L+G750L, while providing enough overlap with JWST (lower limit of 600 nm) to allow for offsets to be applied to match G280 observations to complementary JWST observations. We therefore strongly recommend the use of UVIS/G280 spectroscopy as a powerful UV complement to JWST IR spectroscopy, opening a profound new visual landscape into exoplanet atmospheres from the mid-UV to the mid-IR.

Acknowledgments

This research is based on observations made with the NASA/ESA Hubble Space Telescope obtained from the Space Telescope Science Institute, which is operated by the Association of Universities for Research in Astronomy, Inc., under NASA contract NAS 5-26555. These observations are associated with program HST-GO 17183, PI: H.R. Wakeford. This research has made use of the NASA Exoplanet Archive, which is operated by the California Institute of Technology, under contract with the National Aeronautics and Space Administration under the Exoplanet Exploration Program. V. A.B., N.K.L., S.E.M., M.L-M., M.S.M, and N.E.B., acknowledge support for program number HST-GO-17183 provided through a grant from the STScI under NASA contract NAS 5-26555. C.E.F. acknowledges funding from the University of Bristol School of Physics PhD Scholarship Fund. C.G. acknowledges funding from La Caixa Fellowship and the Agency for Management of University and Research Grants from the Government of Catalonia (FI AGAUR). H.R.W. and D.G. were funded by the UK Research and Innovation (UKRI) framework under the UK government's Horizon Europe funding guarantee for an ERC Starter grant (grant No. EP/Y006313/1). L.A. acknowledges funding from the UKRI STFC Consolidated grant ST/V000454/1. J.K.B. is supported by an STFC Ernest Rutherford Fellowship, grant ST/T004479/1. R.J.M. is supported by NASA through the NASA Hubble Fellowship grant HST-HF2-51513.001, awarded by the Space Telescope Science Institute, which is operated by the Association of Universities for Research in Astronomy, Inc., for NASA, under contract NAS 5-26555. We thank the anonymous reviewer for their swift and insightful feedback.

All the HST data used in this paper can be found in MAST doi:10.17909/yrft-8f93.

Facility: HST (WFC3).

Software: astropy (Astropy Collaboration et al. 2013, 2018), scipy (P. Virtanen et al. 2020), ExoTiC-LD (D. Grant & H. R. Wakeford 2022), ExoTiC-ISM (I. Laginja & H. Wakeford 2020), batman (L. Kreidberg 2015), emcee (D. Foreman-Mackey et al. 2013).

Appendix A
HST WFC3/UVIS G280 Transmission Spectrum of WASP-127b

We present our transmission spectrum of WASP-127b here in Table 5, including the limb-darkening coefficients used in each spectral bin.

Table 5
Atmospheric Transmission Spectrum of WASP-127b Derived from HST WFC3/UVIS G280 Observations and Extracted with `hazelnut`

Wavelength (nm)	Transit Depth (%)	u_1	u_2	u_3	u_4
207.5	1.052 ± 0.207	−0.247	2.203	−4.652	3.654
217.5	1.032 ± 0.119	0.029	1.145	−2.816	2.614
227.5	1.025 ± 0.092	0.326	1.033	−2.318	1.942
237.5	1.168 ± 0.105	0.399	0.213	−1.153	1.528
247.5	1.107 ± 0.095	0.554	−0.579	0.619	0.387
257.5	1.070 ± 0.089	0.323	−0.850	1.942	−0.459
267.5	0.984 ± 0.055	0.751	−1.008	1.275	−0.035
277.5	1.013 ± 0.066	0.466	−0.930	1.879	−0.455
287.5	1.075 ± 0.053	0.355	−0.799	2.089	−0.693
297.5	1.069 ± 0.036	0.312	−0.582	1.896	−0.683
307.5	0.995 ± 0.029	0.313	−0.393	1.595	−0.584
317.5	1.031 ± 0.030	0.230	−0.096	1.374	−0.584
327.5	1.022 ± 0.025	0.457	−0.670	1.845	−0.698
337.5	0.957 ± 0.024	0.410	−0.558	1.876	−0.801
347.5	0.992 ± 0.025	0.491	−0.704	2.013	−0.866
357.5	1.051 ± 0.028	0.339	−0.042	1.220	−0.607
367.5	1.035 ± 0.027	0.584	−0.993	2.285	−0.943
377.5	1.017 ± 0.022	0.758	−1.331	2.285	−0.774
387.5	0.994 ± 0.022	0.642	−0.826	1.799	−0.696
397.5	0.981 ± 0.046	0.373	−0.153	1.263	−0.578
407.5	1.019 ± 0.023	0.421	−0.337	1.472	−0.648
417.5	1.002 ± 0.019	0.555	−0.562	1.481	−0.585
427.5	1.050 ± 0.021	0.522	−0.506	1.529	−0.659
437.5	0.985 ± 0.018	0.374	0.049	0.929	−0.472
447.5	0.980 ± 0.015	0.343	0.217	0.711	−0.399
457.5	1.035 ± 0.019	0.364	0.167	0.760	−0.424
467.5	1.017 ± 0.016	0.359	0.226	0.663	−0.390
477.5	0.975 ± 0.019	0.433	0.064	0.819	−0.467
487.5	0.991 ± 0.017	0.432	0.069	0.773	−0.428
497.5	1.023 ± 0.014	0.449	0.018	0.829	−0.453
507.5	0.973 ± 0.017	0.540	−0.264	1.099	−0.543
517.5	1.025 ± 0.017	0.504	−0.082	0.863	−0.457
527.5	0.993 ± 0.018	0.501	−0.058	0.827	−0.449
537.5	1.020 ± 0.018	0.506	−0.063	0.823	−0.449
547.5	1.011 ± 0.017	0.520	−0.083	0.815	−0.443
557.5	0.974 ± 0.021	0.535	−0.119	0.837	−0.450
567.5	1.003 ± 0.020	0.524	−0.073	0.775	−0.428
577.5	1.012 ± 0.020	0.539	−0.112	0.798	−0.435
587.5	1.035 ± 0.019	0.535	−0.081	0.745	−0.415
597.5	1.000 ± 0.021	0.548	−0.114	0.764	−0.419
607.5	0.999 ± 0.023	0.592	−0.240	0.880	−0.459
617.5	0.991 ± 0.021	0.597	−0.247	0.873	−0.455
627.5	0.995 ± 0.021	0.600	−0.262	0.888	−0.465
637.5	0.992 ± 0.021	0.613	−0.285	0.890	−0.462
647.5	0.934 ± 0.024	0.653	−0.306	0.841	−0.451
657.5	0.970 ± 0.024	0.618	−0.309	0.901	−0.466
667.5	1.029 ± 0.025	0.619	−0.312	0.886	−0.455
677.5	1.002 ± 0.021	0.629	−0.340	0.902	−0.458
687.5	1.040 ± 0.023	0.644	−0.386	0.946	−0.475
697.5	1.029 ± 0.025	0.651	−0.407	0.957	−0.477
707.5	0.977 ± 0.027	0.674	−0.474	1.012	−0.494
717.5	1.034 ± 0.033	0.669	−0.461	0.991	−0.486
727.5	0.965 ± 0.030	0.675	−0.481	1.001	−0.488
737.5	1.010 ± 0.031	0.671	−0.469	0.979	−0.480
747.5	1.022 ± 0.029	0.664	−0.446	0.941	−0.463
757.5	0.932 ± 0.032	0.672	−0.470	0.957	−0.469
767.5	0.980 ± 0.037	0.664	−0.444	0.912	−0.447
777.5	1.028 ± 0.034	0.675	−0.479	0.953	−0.465
787.5	1.013 ± 0.037	0.691	−0.532	1.005	−0.483

Note. We include the central wavelengths for our bins (all with half-width 5 nm) and limb-darkening coefficients (u_i) for our four-parameter nonlinear limb-darkening law.

Appendix B
Retrieved POSEIDON Atmospheric Parameters

We present our POSEIDON model parameters for models A through M in Table 6, including abundances of each species as well as constraints on aerosols.

Table 6
Median and 1σ Errors of Atmospheric Parameters for Each POSEIDON Retrieval Model

Model	$\log X_{\rm Na}$	$\log X_{\rm K}$	$\log X_{\rm H_2O}$	$\log X_{\rm CO_2}$	$\log X_{\rm CO}$	$\log X_{\rm CH_4}$	$\log X_{\rm FeH}$
A	$-8.13^{+1.53}_{-2.14}$	$-9.50^{+1.95}_{-1.58}$	$-7.17^{+3.62}_{-3.07}$	⋯	⋯	⋯	⋯
B	⋯	$-9.57^{+1.93}_{-1.54}$	$-6.93^{+3.61}_{-3.30}$	⋯	⋯	⋯	⋯
C	$-8.05^{+1.42}_{-2.07}$	$-9.67^{+1.93}_{-1.47}$	$-6.90^{+3.53}_{-3.18}$	⋯	⋯	⋯	$-7.75^{+2.43}_{-2.63}$
D	$-7.28^{+0.37}_{-0.44}$	$-9.42^{+0.93}_{-1.36}$	$-3.89^{+0.20}_{-0.17}$	$-4.75^{+0.39}_{-0.38}$	$-6.40^{+2.71}_{-3.78}$	$-10.09^{+1.47}_{-1.28}$	⋯
E	⋯	$-9.92^{+0.94}_{-1.22}$	$-3.99^{+0.20}_{-0.17}$	$-4.84^{+0.39}_{-0.42}$	$-6.09^{+2.43}_{-3.77}$	$-10.14^{+1.36}_{-1.25}$	⋯
F	$-7.21^{+0.34}_{-0.39}$	$-9.74^{+1.02}_{-1.27}$	$-3.91^{+0.18}_{-0.17}$	$-4.82^{+0.37}_{-0.42}$	$-6.43^{+2.63}_{-3.78}$	$-10.04^{+1.44}_{-1.32}$	$-8.29^{+0.56}_{-1.07}$
G	$-8.08^{+1.54}_{-2.46}$	$-9.69^{+1.77}_{-1.55}$	$-3.06^{+0.70}_{-0.45}$	$-4.52^{+0.91}_{-0.69}$	$-7.37^{+3.23}_{-3.10}$	$-9.47^{+1.77}_{-1.69}$	⋯
H	⋯	$-9.72^{+1.79}_{-1.53}$	$-3.03^{+0.65}_{-0.45}$	$-4.48^{+0.85}_{-0.69}$	$-7.36^{+3.27}_{-3.10}$	$-9.47^{+1.81}_{-1.71}$	⋯
I	$-8.06^{+1.38}_{-2.41}$	$-9.95^{+1.68}_{-1.37}$	$-3.14^{+0.60}_{-0.39}$	$-4.70^{+0.84}_{-0.63}$	$-7.24^{+3.27}_{-3.19}$	$-9.47^{+1.82}_{-1.69}$	$-7.17^{+0.70}_{-1.07}$
J	$-7.38^{+0.91}_{-2.07}$	$-9.74^{+1.67}_{-1.51}$	$-3.55^{+0.36}_{-0.30}$	$-4.94^{+0.63}_{-0.59}$	$-7.41^{+3.15}_{-3.11}$	$-9.77^{+1.63}_{-1.47}$	⋯
K	⋯	$-9.79^{+1.71}_{-1.48}$	$-3.56^{+0.37}_{-0.30}$	$-4.91^{+0.63}_{-0.60}$	$-7.44^{+3.15}_{-3.07}$	$-9.74^{1.66}_{-1.52}$	⋯
L	$-7.25^{+0.72}_{-1.41}$	$-9.92^{+1.61}_{-1.38}$	$-3.60^{+0.29}_{-0.26}$	$-4.97^{+0.56}_{-0.55}$	$-7.42^{+3.17}_{-3.07}$	$-9.75^{+1.57}_{-1.47}$	$-8.10^{+0.77}_{-1.92}$
M	$-7.36^{+0.42}_{-0.48}$	$-9.82^{+0.90}_{-1.26}$	$-4.05^{+0.18}_{-0.17}$	$-5.13^{+0.41}_{-0.48}$	$-6.65^{+2.82}_{-3.54}$	$-10.04^{+1.32}_{-1.28}$	$-8.15^{+0.44}_{-0.72}$

Model	$R_{\rm P_{ref}}$ ($R_{\rm J}$)	T (K)	$\log a$	γ	$\log P_{\rm cloud}$	$\bar{\phi}_{\rm cloud}$	$\delta_{\rm rel}$ (ppm)
A	$1.19^{+0.03}_{-0.04}$	$565.0^{+201.0}_{-113.2}$	$-0.78^{+2.50}_{-2.01}$	$-8.48^{+7.51}_{-7.31}$	$-3.73^{+1.33}_{-1.39}$	$0.72^{+0.16}_{-0.22}$	⋯
B	$1.18^{+0.03}_{-0.04}$	$573.0^{+201.6}_{-118.8}$	$-0.77^{+2.50}_{-2.02}$	$-7.94^{+7.07}_{-7.61}$	$-3.74^{+1.24}_{-1.41}$	$0.74^{+0.15}_{-0.20}$	⋯
C	$1.19^{+0.03}_{-0.04}$	$550.2^{+188.7}_{-103.1}$	$-0.73^{+2.52}_{-2.04}$	$-8.12^{+6.92}_{-7.37}$	$-3.74^{+1.36}_{-1.36}$	$0.68^{+0.18}_{-0.24}$	⋯
D	$1.19^{+0.02}_{-0.02}$	$770.7^{+59.5}_{-69.9}$	$-1.59^{+2.01}_{-1.64}$	$-8.24^{+6.93}_{-7.58}$	$-4.07^{+1.12}_{-1.74}$	$0.35^{+0.08}_{-0.07}$	$-195.05^{+38.29}_{-40.59}$
E	$1.20^{+0.02}_{-0.02}$	$751.1^{+62.6}_{-73.7}$	$-1.75^{+1.80}_{-1.49}$	$-8.26^{+6.93}_{-7.28}$	$-3.66^{+0.92}_{-1.87}$	$0.34^{+0.10}_{-0.09}$	$-190.79^{+37.12}_{-39.37}$
F	$1.18^{+0.02}_{-0.02}$	$797.3^{+54.4}_{-68.4}$	$-1.33^{+2.07}_{-1.74}$	$-8.26^{+6.87}_{-7.62}$	$-4.67^{+1.39}_{-1.58}$	$0.31^{+0.08}_{-0.07}$	$-190.24^{+39.94}_{-38.61}$
G	$1.14^{+0.02}_{-0.01}$	$968.1^{+102.5}_{-93.1}$	$-2.02^{+1.53}_{-1.32}$	$-8.28^{+6.38}_{-7.12}$	$-2.87^{+0.37}_{-0.57}$	$0.92^{+0.06}_{-0.10}$	$144.25^{+59.15}_{-58.39}$
H	$1.14^{+0.02}_{-0.01}$	$965.3^{+99.7}_{-93.2}$	$-2.05^{+1.51}_{-1.31}$	$-8.23^{+6.45}_{-7.13}$	$-2.90^{+0.38}_{-0.53}$	$0.92^{+0.06}_{-0.10}$	$154.59^{+55.51}_{-55.37}$
I	$1.13^{+0.02}_{-0.01}$	$1005.6^{+101.8}_{-94.2}$	$-2.10^{+1.49}_{-1.26}$	$-8.07^{+6.31}_{-7.18}$	$-2.87^{+0.36}_{-0.56}$	$0.87^{+0.09}_{-0.14}$	$191.85^{+68.56}_{-69.81}$
J	$1.16^{+0.02}_{-0.02}$	$946.5^{+123.5}_{-117.4}$	$-2.00^{+2.16}_{-1.37}$	$-5.82^{+4.88}_{-8.50}$	$-2.50^{+0.29}_{-0.42}$	$0.86^{+0.10}_{-0.14}$	⋯
K	$1.16^{+0.02}_{-0.02}$	$941.2^{+122.1}_{-118.4}$	$-1.93^{+2.36}_{-1.41}$	$-5.06^{+4.25}_{-9.07}$	$-2.49^{+0.29}_{-0.42}$	$0.87^{+0.10}_{-0.16}$	⋯
L	$1.16^{+0.02}_{-0.02}$	$941.3^{+113.7}_{-107.6}$	$-2.08^{+1.69}_{-1.30}$	$-7.22^{+5.95}_{-7.79}$	$-2.64^{+0.38}_{-0.78}$	$0.72^{+0.18}_{-0.22}$	⋯
M	$1.18^{+0.02}_{-0.02}$	$829.5^{+75.0}_{-68.6}$	$-0.58^{+2.60}_{-2.20}$	$-9.37^{+6.99}_{-7.10}$	$-4.95^{+1.46}_{-1.36}$	$0.26^{+0.06}_{-0.05}$	⋯

ORCID iDs

V. A. Boehm https://orcid.org/0000-0002-4945-1860
N. K. Lewis https://orcid.org/0000-0002-8507-1304
C. E. Fairman https://orcid.org/0000-0001-9665-5260
S. E. Moran https://orcid.org/0000-0002-6721-3284
C. Gascón https://orcid.org/0000-0001-5097-9251
H. R. Wakeford https://orcid.org/0000-0003-4328-3867
M. K. Alam https://orcid.org/0000-0003-4157-832X
L. Alderson https://orcid.org/0000-0001-8703-7751
J. Barstow https://orcid.org/0000-0003-3726-5419
N. E. Batalha https://orcid.org/0000-0003-1240-6844
D. Grant https://orcid.org/0000-0001-5878-618X
M. López-Morales https://orcid.org/0000-0003-3204-8183
R. J. MacDonald https://orcid.org/0000-0003-4816-3469
Mark S. Marley https://orcid.org/0000-0002-5251-2943
K. Ohno https://orcid.org/0000-0003-3290-6758

References

Ackerman, A. S., & Marley, M. S. 2001, ApJ, 556, 872
Ahrer, E.-M., Stevenson, K. B., Mansfield, M., et al. 2023, Natur, 614, 653
Alderson, L., Wakeford, H. R., Alam, M. K., et al. 2023, Natur, 614, 664
Allart, R., Pino, L., Lovis, C., et al. 2020, A&A, 644, A155
Astropy Collaboration, Price-Whelan, A. M., Sipőcz, B. M., et al. 2018, AJ, 156, 123
Astropy Collaboration, Robitaille, T. P., Tollerud, E. J., et al. 2013, A&A, 558, A33
Batalha, N., Rooney, C., & Mukherjee, S. 2020, natashabatalha/virga: Initial Release, v0.0, Zenodo, doi:10.5281/zenodo.3759888
Batalha, N. E., Marley, M. S., Lewis, N. K., & Fortney, J. J. 2019, ApJ, 878, 70
Boucher, A., Lafreniere, D., Pelletier, S., et al. 2023, MNRAS, 522, 5062
Buchner, J., Georgakakis, A., Nandra, K., et al. 2014, A&A, 564, A125
Chen, G., Pallé, E., Welbanks, L., et al. 2018, A&A, 616, A145
Evans, T. M., Sing, D. K., Goyal, J. M., et al. 2018, AJ, 156, 283
Fairman, C., Wakeford, H. R., & MacDonald, R. J. 2024, AJ, 167, 240
Feinstein, A. D., Radica, M., Welbanks, L., et al. 2023, Natur, 614, 670
Feroz, F., & Hobson, M. P. 2008, MNRAS, 384, 449
Flagg, L., Turner, J. D., Deibert, E., et al. 2023, ApJL, 953, L19
Foreman-Mackey, D., Hogg, D. W., Lang, D., & Goodman, J. 2013, PASP, 125, 306
Freedman, R. S., Marley, M. S., & Lodders, K. 2008, ApJS, 174, 504
Gao, P., Thorngren, D. P., Lee, E. K. H., et al. 2020, NatAs, 4, 951
Gharib-Nezhad, E., Iyer, A. R., Line, M. R., et al. 2021, ApJS, 254, 34
Gibson, N. P., Nikolov, N., Sing, D. K., et al. 2017, MNRAS, 467, 4591
Grant, D., Lewis, N. K., Wakeford, H. R., et al. 2023, ApJL, 956, L32
Grant, D., Exo-TiC/ExoTiC-LD: ExoTiC-LD v3.0.0, Zenodo, doi:10.5281/zenodo.7437681
Grant, D., & Wakeford, H. 2024, JOSS, 9, 6816
Guillot, T. 2010, A&A, 520, A27
Horne, K. 1986, PASP, 98, 609
JWST Transiting Exoplanet Community Early Release Science Team, Ahrer, E.-M., Alderson, L., et al. 2023, Natur, 614, 649
Kanumalla, K., Line, M. R., Weiner Mansfield, M., et al. 2024, AJ, 168, 201
Kawashima, Y., & Ikoma, M. 2019, ApJ, 877, 109
Kempton, E. M.-R., & Knutson, H. A. 2024, RvMG, 90, 411
Kreidberg, L. 2015, PASP, 127, 1161
Laginja, I., & Wakeford, H. 2020, JOSS, 5, 2281
Lam, K. W. F., Faedi, F., Brown, D. J. A., et al. 2017, A&A, 599, A3
Lavvas, P., & Koskinen, T. 2017, ApJ, 847, 32
Li, G., Gordon, I. E., Rothman, L. S., et al. 2015, ApJS, 216, 15
Lodders, K. 2010, in Principles and Perspectives in Cosmochemistry16ed. Aruna Goswami & B. Eswar Reddy (Berlin: Springer), 379
Lothringer, J. D., Sing, D. K., Rustamkulov, Z., et al. 2022, Natur, 604, 49
Lupu, R., Freedman, R., Gharib-Nezhad, E., Visscher, C., & Molliere, P. 2021, Correlated k coefficients for H2-He atmospheres; 196 spectral windows and 1460 pressure-temperature points, v1, Zenodo, doi:10.5281/ZENODO.5590989
MacDonald, R. J. 2023, JOSS, 8, 4873
MacDonald, R. J., & Madhusudhan, N. 2017, MNRAS, 469, 1979
MacDonald, R. J., & Madhusudhan, N. 2019, MNRAS, 486, 1292
Magic, Z., Chiavassa, A., Collet, R., & Asplund, M. 2015, A&A, 573, A90
Mandel, K., & Agol, E. 2002, ApJL, 580, L171
Marley, M. S., Saumon, D., Visscher, C., et al. 2021, ApJ, 920, 85
Marsh, T. R. 1989, PASP, 101, 1032
McCullough, P. R., Crouzet, N., Deming, D., & Madhusudhan, N. 2014, ApJ, 791, 55
Morley, C. V., Fortney, J. J., Marley, M. S., et al. 2012, ApJ, 756, 172
Mukherjee, S., Batalha, N. E., Fortney, J. J., & Marley, M. S. 2023, ApJ, 942, 71
Nortmann, L., Lesjak, F., Yan, F., et al. 2024, arXiv:2404.12363
Ohno, K., & Kawashima, Y. 2020, ApJL, 895, L47
Ohno, K., Okuzumi, S., & Tazaki, R. 2020, ApJ, 891, 131
Ormel, C. W., & Min, M. 2019, A&A, 622, A121
Palle, E., Chen, G., Prieto-Arranz, J., et al. 2017, A&A, 602, L15
Parmentier, V., Fortney, J. J., Showman, A. P., Morley, C., & Marley, M. S. 2016, ApJ, 828, 22
Pinhas, A., & Madhusudhan, N. 2017, MNRAS, 471, 4355
Pirzkal, N. 2020, Instrument Science Report WFC3 2020-9, Space Telescope Science Institute
Pirzkal, N., & Ryan, R. 2017, Instrument Science Report WFC3 2017-01 (v.1), Space Telescope Science Institute
Polyansky, O. L., Kyuberis, A. A., Zobov, N. F., et al. 2018, MNRAS, 480, 2597
Pont, F., Sing, D. K., Gibson, N. P., et al. 2013, MNRAS, 432, 2917
Powell, D., Louden, T., Kreidberg, L., et al. 2019, ApJ, 887, 170
Rooney, C. M., Batalha, N. E., Gao, P., & Marley, M. S. 2022, ApJ, 925, 33
Rustamkulov, Z., Sing, D. K., Mukherjee, S., et al. 2023, Natur, 614, 659
Ryabchikova, T., Piskunov, N., Kurucz, R. L., et al. 2015, PhyS, 90, 054005
Sharp, C. M., & Burrows, A. 2007, ApJS, 168, 140
Sing, D. K., Lavvas, P., Ballester, G. E., et al. 2019, AJ, 158, 91
Sing, D. K., Wakeford, H. R., Showman, A. P., et al. 2015, MNRAS, 446, 2428
Skaf, N., Bieger, M. F., Edwards, B., et al. 2020, AJ, 160, 109
Sotzen, K. S., Stevenson, K. B., Sing, D. K., et al. 2020, AJ, 159, 5
Spake, J. J., Sing, D. K., Wakeford, H. R., et al. 2021, MNRAS, 500, 4042
Steinrueck, M. E., Koskinen, T., Lavvas, P., et al. 2023, ApJ, 951, 117
Tashkun, S. A., & Perevalov, V. I. 2011, JQSRT, 112, 1403
Thorngren, D., Gao, P., & Fortney, J. J. 2019, ApJL, 884, L6
van Dokkum, P. G. 2001, PASP, 113, 1420
Virtanen, P., Gommers, R., Oliphant, T. E., et al. 2020, NatMe, 17, 261
Visscher, C., Lodders, K., Fegley, & Bruce, J. 2010, ApJ, 716, 1060
Wakeford, H., Alderson, L., Batalha, N., et al. 2022, HST Proposal, 17183
Wakeford, H. R., & Sing, D. K. 2015, A&A, 573, A122
Wakeford, H. R., Sing, D. K., Deming, D., et al. 2018, AJ, 155, 29
Wakeford, H. R., Sing, D. K., Evans, T., Deming, D., & Mandell, A. 2016, ApJ, 819, 10
Wakeford, H. R., Sing, D. K., Stevenson, K. B., et al. 2020, AJ, 159, 204
Wakeford, H. R., Visscher, C., Lewis, N. K., et al. 2017, MNRAS, 464, 4247
Wende, S., Reiners, A., Seifahrt, A., & Bernath, P. 2010, A&A, 523, A58
Wilson, T. J. 2021, RNASS, 5, 265
Woitke, P., Helling, C., Hunter, G. H., et al. 2018, A&A, 614, A1
Yurchenko, S. N., Amundsen, D. S., Tennyson, J., & Waldmann, I. P. 2017, A&A, 605, A95
Žák, J., Kabáth, P., Boffin, H. M. J., Ivanov, V. D., & Skarka, M. 2019, AJ, 158, 120